Rapid O$_3$ assimilations – Part 1: background and local contributions to tropospheric O$_3$ changes in China in 2015-2020

Rui Zhu[1], Zhaojun Tang[1], Xiaokang Chen[1], Xiong Liu[2] and Zhe Jiang[1]*

[1]School of Earth and Space Sciences, University of Science and Technology of China, Hefei, Anhui, 230026, China.
[2]Center for Astrophysics | Harvard & Smithsonian, Cambridge, MA 02138, USA.

*Correspondence to: Zhe Jiang (zhejiang@ustc.edu.cn)

Abstract

A single ozone (O$_3$) tracer mode was developed in this work to build the capability of the GEOS-Chem model for rapid O$_3$ simulation. The single O$_3$ tracer simulation demonstrates consistency with the GEOS-Chem full chemistry simulation, with dramatic reductions in computational costs of approximately 91-94%. The single O$_3$ tracer simulation was combined with surface and Ozone Monitoring Instrument (OMI) O$_3$ observations to investigate the changes in tropospheric O$_3$ over eastern (E.) China in 2015-2020. The assimilated O$_3$ concentrations demonstrate good agreement with O$_3$ observations: surface O$_3$ concentrations are 43.2, 41.8 and 42.1 ppb, and tropospheric O$_3$ columns are 37.1, 37.9 and 38.0 DU in the simulations, assimilations and observations, respectively. The assimilations indicate rapid rises in surface O$_3$ concentrations by 1.60 (spring), 1.16 (summer), 1.47 (autumn) and 0.80 (winter) ppb yr^{-1} over E. China in 2015-2020, and the increasing trends are underestimated by the a priori simulations. More attention is suggested to the rapid increases in O$_3$ pollution in spring and autumn. We find stronger rises in tropospheric O$_3$ columns over highly polluted areas due to larger local contributions, for example, 0.12 DU yr^{-1} (North China Plain) in contrast to -0.29 (Sichuan Basin) -0.25 DU yr^{-1} (Southern China). Furthermore, our analysis demonstrated noticeable contributions of the interannual variability in background O$_3$ to the trends in surface O$_3$ (particularly in the summer) and tropospheric O$_3$ columns over E. China in 2015-2020. This work highlights the importance of rapid simulations and assimilations to extend and interpret

32   atmospheric O_3 observations.

1. Introduction

35   Tropospheric ozone (O_3) is produced when volatile organic compounds (VOCs) and

36   carbon monoxide (CO) are photochemically oxidized in the presence of nitrogen oxides (NO_x).

37   Tropospheric O_3 has important influences on the climate (Mickley, 2004; Iglesias-Suarez et al.,

38   2018), atmospheric oxidation capacity (Thompson, 1992; Prinn, 2003), human health and crop

39   growth (Zhang et al., 2021; Li et al., 2022). The important role of O_3 in the atmosphere has led

40   to many efforts focusing on O_3 observations that have improved our understanding of

41   atmospheric O_3 (Logan et al., 2012; Oetjen et al., 2016; Parrish et al., 2021). The limited spatial

42   coverage of O_3 observations promotes the efforts of spatial extensions of O_3 observations

43   (Chang et al., 2015; Peng et al., 2016). Recent advances in machine learning techniques further

44   provide a new method to extend O_3 observations by fusing satellite and surface observations

45   (Li et al., 2020; Liu et al., 2022; Wei et al., 2022).

46   Chemical transport models (CTMs), as powerful tools, have been widely used to simulate

47   and interpret observed O_3 variabilities (Parrington et al., 2012; Jiang et al., 2016; Li, Ke et al.,

48   2019). Despite the advances in CTMs, an accurate simulation of observed O_3 is still challenging

49   because of uncertainties in physical and chemical processes (Peng et al., 2021; Chen et al.,

50   2022), emission inventories (Elguindi et al., 2020; Jiang et al., 2022) and coarse model

51   resolutions (Schaap et al., 2015; Benavides et al., 2021). Furthermore, the high computational

52   cost is a bottleneck for rapid simulations, which poses a possible barrier to better understanding

53   tropospheric O_3. Alternatively, researchers may consider simulations of atmospheric O_3 with

54   the archived O_3 product and loss rates. For example, the tagged-O_x mode of the GEOS-Chem

55   model has been used to analyze the sources and transport of tropospheric O_3 (Zhang et al., 2008;

56   Zhu et al., 2017; Han et al., 2018). However, it may not be an ideal choice to perform O_3

57   simulations based on the tagged-O_x mode because O_x is the combination of multiple species

58   ($O_x=O_3+NO_2+2NO_3+3N_2O_5+HNO_3+HNO_4+peroxyacylnitrates$) and thus cannot be accurately

59   compared with O_3 observations.

60   In this study, we developed the single O_3 tracer mode (tagged-O_3) of the GEOS-Chem

61   model, driven by archived O_3 product and loss rates provided by GEOS-Chem full chemistry

62   simulations, to build the capability of the GEOS-Chem model for rapid simulations of

63   tropospheric O_3 (rather than O_x). Data assimilations, by combining modeled and observed O_3

64   concentrations, can take advantage of both simulations and observations to produce more

65   accurate O_3 concentrations (Parrington et al., 2008; Ma et al., 2019; Huijnen et al., 2020). The

66   single O_3 tracer simulations were thus further combined with the Ozone Monitoring Instrument

67   (OMI) and China Ministry of Ecology and Environment (MEE) monitoring network O_3

68   observations (in this paper) and United States (US) Air Quality System (AQS) and European

69   AirBase network O_3 observations (in the companion paper, (Zhu et al., 2023)) via a sequential

70   Kalman Filter (KF) assimilation system (Tang et al., 2022; Han et al., 2022) to perform a

71   comparative analysis to investigate the changes in tropospheric O_3 in eastern (E.) China in

72   2015-2020 (in this paper) and the US and Europe in 2005-2020 (Zhu et al., 2023).

73   Satellite instruments provide globally covered O_3 observations that are sensitive to O_3

74   concentrations in the free troposphere. The OMI-based assimilations can thus reflect the

75   optimized adjustments in both global background and local O_3 concentrations. On the other

76   hand, surface observations are sensitive to local O_3 concentrations. Surface observation-based

77   assimilations can reflect the optimized adjustments in local contributions, and the information

78   of local contributions can be transported into the free troposphere via vertical convection in the

79   assimilation processes, which is different from the fusion of satellite and surface observations

80   (Li et al., 2020; Liu et al., 2022; Wei et al., 2022). Consequently, a comparative analysis by

81   assimilating satellite and surface O_3 observations is useful for better characterization of O_3

82   changes in the surface and free troposphere. Furthermore, the low computational costs of the

83   single O_3 tracer simulations allow us to design and perform different experiments much more

84   efficiently. Multiple simulation and assimilation experiments (see details in Table 1) were thus

85   conducted in this work to analyze the impacts of background O_3 (particularly, the interannual

86   and seasonal variabilities in the background O_3 as well as optimization in the background O_3)

87   and local O_3 formation on the changes in surface and free tropospheric O_3 over E. China.

88   This paper is organized as follows: in Section 2, we provide descriptions of the MEE and

89   OMI O_3 observations, the GEOS-Chem model and the single O_3 tracer simulation and

90   assimilation system used in this work. Tropospheric O_3 changes in E. China in 2015-2020 are

91   then demonstrated in Section 3 by assimilating MEE and OMI O_3 observations. As shown in

92   Fig. 1, five regions (i.e., North China Plain (#1), Yangtze River Delta (#2), Central China (#3),

93   Sichuan Basin (#4) and Southern China (#5)) are defined within the E. China domain. Regions

94   #1 and #2 are defined as highly polluted regions by excluding grids with low and medium

95   anthropogenic NO_x emissions. Tropospheric O_3 changes over these regions are discussed to

96   investigate the possible regional discrepancies in surface and free tropospheric O_3 associated

97   with different local pollution levels. Our conclusions follow in Section 4.

98

99   2. Data and Methods

100   2.1 Surface O_3 measurements

101   We use MEE surface in situ O_3 concentration data (https://quotsoft.net/air/) for the period

102   2015-2020. These real-time monitoring stations report hourly concentrations of criteria

103   pollutants from 1691 sites in 2020. All stations (1441 urban sites and 250 urban background

104   sites) are assimilated in our analysis. Concentrations were reported by the MEE in $\mu g\ m^{-3}$ under

105   standard temperature (273 K) until 31 August 2018. This reference state was changed on 1

106   September 2018 to 298 K. We converted the O_3 concentrations to ppb and rescaled the post-

107 August 2018 concentrations to the standard temperature (273 K) to maintain consistency in the

108 trend analysis. It should be noted that the assimilation of O_3 observations from urban and urban

109 background sites may result in possible overestimation of surface O_3 concentrations over rural

110 areas.

111 **2.2 OMI PROFOZ product**

112 The OMI instrument was launched in July 2004 on the Aura spacecraft with a spatial

113 resolution of 13 × 24 km (nadir view). It provides globally covered measurements with

114 backscattered sunlight in the ultraviolet–visible range from 270 to 500 nm (UV1: 270–310 nm;

115 UV2: 310–365 nm; visible: 350–500 nm). In this study, we use the OMI O_3 profile retrieval

116 product (PROFOZ v0.9.3, level 2, Liu et al. (2010); Huang et al. (2017)) from the Smithsonian

117 Astrophysical Observatory (SAO). The retrieval uses the vector linearized discrete ordinate

118 radiative transfer model (VLIDORT) (Spurr, 2006) and Bayesian optimal estimation. Profiles

119 of partial O_3 columns (unit: DU) are retrieved in the spectral region of 270–330 nm with 24

120 vertical layers: approximately 2.5 km for each layer from the surface to approximately 60 km.

121 The following filters are applied in our analysis following Huang et al. (2017): 1) nearly clear-

122 sky scenes with effective cloud fraction < 0.3; 2) solar zenith angles (SZA) < 75°; and 3) fitting

123 root mean square (RMS, ratio of fitting residuals to assumed measurement error) < 2.0.

124 Starting in 2009, anomalies were found in the OMI data and diagnosed as attenuated

125 measured radiances in certain cross-track positions. This instrument degradation has been

126 referred to as the "row anomaly". To enhance the quality and stability of the data, only across-

127 track positions between 4-11 (within 30 positions in the UV1 channels) are assimilated in our

128 main assimilation experiment (Exp. #8). This treatment is similar to the production of row-

129 isolated data by using across-track positions between 3-18 (within 60 positions in the UV2

130 channels) in the OMI/MLS O_3 data (Ziemke et al., 2019; Wang, X. et al., 2022). The effects of

131 the usage of row-isolated data will be evaluated by comparing the main assimilation experiment

132   with the sensitivity assimilation experiment (Exp. #10) by assimilating OMI O_3 observations

133   at across-track positions 4-27.

134   The modeled tropospheric O_3 profiles in the assimilation processes and subsequent

135   analyses are convolved by using the OMI retrieval averaging kernels and a priori O_3 profile

136   based on the following equation (Liu et al., 2010; Huang et al., 2017):

137 $$\hat{x} = x_a + A(x - x_a) \qquad \text{(Eq. 1)}$$

138   where $\hat{x}$ is the modeled O_3 profile convolved by the retrieval averaging kernels, x_a is the

139   OMI a priori O_3 profile, x is the modeled O_3 profile, and A is the OMI averaging kernel

140   matrix. Here $A(i,j) = \frac{\partial \hat{x}_j}{\partial x_i}$, representing the sensitivity of the retrieved partial O_3 column (DU)

141   at layer j to the change in O_3 (DU) at layer i. The unit for averaging kernels in this OMI product

142   is DU/DU because the conversion from DU to ppb varies with altitude.

143   **2.3 GEOS-Chem model configuration**

144   The GEOS-Chem chemical transport model (http://www.geos-chem.org, version 12-8-1)

145   is driven by assimilated meteorological data from MERRA-2. The GEOS-Chem full chemistry

146   simulation includes fully coupled O_3-NO_x-VOC-halogen-aerosol chemistry. Our analysis is

147   conducted at a horizontal resolution of nested 0.5°×0.625° over E. China with chemical

148   boundary conditions archived every 3 hours from global simulations with 4°×5° resolution.

149   Emissions are computed by the Harvard-NASA Emission Component (HEMCO). Global

150   default anthropogenic emissions are from the CEDS (Community Emissions Data System)

151   (Hoesly et al., 2018). Regional emissions are replaced by MEIC (Multiresolution Emission

152   Inventory for China) in China and MIX in other regions of Asia (Li et al., 2017). The reference

153   year for the CEDS inventory is 2010 with annual scaling factors in 2005-2014, and the

154   reference year for the MEIC/MIX inventory is 2010 with annual scaling factors in 2008-2010

155   in the GEOS-Chem model. Open fire emissions are from the Global Fire Emissions Database

156   (GFED4) (van der Werf et al., 2010).

157   Following Jiang et al. (2022), the total anthropogenic NO_x and VOC emissions in the

158   GEOS-Chem model are scaled based on Zheng et al. (2018) and Li, M. et al. (2019) so that the

159   modeled surface nitrogen dioxide (NO_2) and O_3 concentrations in the a priori simulations are

160   identical to Jiang et al. (2022) in 2005-2018. The total anthropogenic NO_x and VOC emissions

161   in 2019-2020 are further scaled based on linear projections. The total anthropogenic NO_x

162   emissions in the a priori simulations declined by 19% in China in 2015-2020. The total

163   anthropogenic VOC emissions in the a priori simulations increased by 1% in China in 2015-

164   2020. We refer the reader to Jiang et al. (2022) for the details of the model configuration and

165   performance, particularly the modeled trends of surface and tropospheric column NO_2 in 2005-

166   2018.

167   **2.4 Single O_3 tracer simulation**

168   A new chemical mechanism was developed in this work to allow the running of the single

169   O_3 tracer mode (tagged-O_3). As shown in Fig. S1 (see the SI), the package of the Kinetic

170   PreProcessor (KPP) module was modified to define the production (PO_3) and loss (LO_3) of O_3.

171   The GEOS-Chem full chemistry simulations with the updated KPP module were then

172   performed to produce PO_3 (unit kg cm^{-3} s^{-1}) and relative LO_3 (i.e., $LO_3/[O_3]$ with unit cm^{-3} s^{-1})

173   every 20 minutes. Here the 20 minutes are selected to be the same as the chemical time step in

174   the GEOS-Chem full chemistry mode to ensure consistency between the single O_3 tracer and

175   full chemistry simulations. The single O_3 tracer simulation (tagged_o3_mod.F90) was then

176   performed by reading the archived PO_3 and relative LO_3. Because we are interested in

177   tropospheric chemistry, we archived O_3 concentrations instead of O_3 production and loss rates

178   in the stratosphere in the full chemistry simulations. The archived stratospheric O_3

179   concentrations were read in the single O_3 tracer simulation process as boundary conditions to

180   ensure a reasonable stratospheric-tropospheric O_3 exchange.

181   The major advantage of the single O_3 tracer simulation is dramatic reductions in

182 computational costs by approximately 91%-94%; for example, the computational costs (hours

183 of wall time for one year simulation) are 57.5 and 5.2 hours at the global scale (4°×5°) and 80.2

184 and 4.5 hours within the nested China domain (0.5°×0.625°) by full chemistry and single O_3

185 tracer simulations, respectively. Consequently, once PO_3 and LO_3 are produced, the

186 computational costs of performing additional single O_3 tracer simulations are almost negligible.

187 The low computational costs of the single O_3 tracer simulation allow us to design and perform

188 different simulation and assimilation experiments much more efficiently. As shown in Table

189 1, there are 10 different simulation and assimilation experiments performed in this work, which

190 requires 4812 hours (wall time) with the full chemistry simulation but only 270 hours (wall

191 time) with the single O_3 tracer simulation.

192 Here we evaluate the consistency in modeled O_3 concentrations between single O_3 tracer

193 and full chemistry simulations. Fig. 2A1-A5 show the annual and seasonal averages of the

194 surface maximum daily 8-hour average (MDA8) O_3 over E. China in 2015-2020 from the full

195 chemistry simulation. The modeled surface MDA8 O_3 concentrations are as high as 60-70 ppb

196 in the summer and as low as 10-20 ppb in the winter over northern China. The simulation with

197 the single O_3 tracer mode (Fig. 2B1-B5) demonstrates spatial consistency with the full

198 chemistry simulation (Fig. 2A1-A5) and temporal consistency at both the daily (Fig. 3A) and

199 monthly (Fig. 3B) scales in 2015-2020. In contrast, the tagged-O_x mode of the GEOS-Chem

200 model is driven by the archived production and loss of O_x, which is the combination of multiple

201 species including O_3. There are large discrepancies between full chemistry (Fig. 2A1-A5) and

202 tagged-O_x (Fig. 2C1-C5) simulations. As shown in Fig. 3, the O_x concentrations are higher than

203 the O_3 concentrations by approximately 6 ppb, and the relative difference can reach 40% in the

204 winter. Our analysis thus indicates the reliability of the single O_3 tracer simulations developed

205 in this work.

206 **2.5 Data assimilation method**

207   We employ the sequential KF to assimilate O_3 observations, which has been used in

208   recent studies to optimize tropospheric CO concentrations (Tang et al., 2022; Han et al., 2022).

209   As a brief description of the assimilation algorithm, the forward model ($\mathbf{M}$) predicts the O_3

210   concentration ($\boldsymbol{x}_{at}$) at time t:

211    $$\boldsymbol{x}_{at} = \mathbf{M}_t \boldsymbol{x}_{t-1} \quad (\text{Eq.}\,2)$$

212   The optimized O_3 concentrations can be expressed as:

213    $$\boldsymbol{x}_t = \boldsymbol{x}_{at} + \mathbf{G}_t(\boldsymbol{y}_t - \mathbf{K}_t \boldsymbol{x}_{at}) \quad (\text{Eq.}\,3)$$

214   where $\boldsymbol{y}_t$ is the observation and $\mathbf{K}_t$ represents the operation operator that projects O_3

215   concentrations from the model space to the observation space. $\mathbf{G}_t$ is the KF gain matrix, which

216   can be described as:

217    $$\mathbf{G}_t = \mathbf{S}_{at}\mathbf{K}_t^T(\mathbf{K}_t\mathbf{S}_{at}\mathbf{K}_t^T + \mathbf{S}_\epsilon)^{-1} \quad (\text{Eq.}\,4)$$

218   where $\mathbf{S}_{at}$ and $\mathbf{S}_\epsilon$ are the model and observation covariances, respectively. The optimized O_3

219   concentrations provided by Eq. 3 are then forwarded (hourly) to Eq. 2. The model errors are

220   assumed to be 50% because the objective of our assimilations is to provide dynamic extensions

221   of atmospheric O_3 observations. The a posteriori O_3 concentrations with the assumption of 50%

222   model errors are expected to match better with atmospheric O_3 observations. The measurement

223   errors are calculated as $\varepsilon_0 = ermax + 0.0075 * \Pi_0$, where *ermax* is the base error (1.5 µg m^{-}

224   ^{3}) and Π_0 represents the observed O_3 concentrations (unit: µg m^{-3}). The representation errors

225   are calculated as $\varepsilon_r = \gamma\varepsilon_0\sqrt{\Delta l/L}$, where γ is a scaling factor (0.5), Δl is the model resolution

226   (~56 km in this study), and L represents the range that the observation can reflect, which

227   depends on the station type (2 km for urban, 4 km for suburban). The total observation error is

228   then defined as $\varepsilon_t = \sqrt{\varepsilon_0^2 + \varepsilon_r^2}$. Furthermore, the "superobservation" method was applied in

229   this work to further reduce the influence of representative error (Miyazaki et al., 2017; Tang et

230   al., 2022):

231    $$\omega_j = 1/\varepsilon_j^2 \quad (\text{Eq.}\,5)$$

232     $$y_s = \sum_{j=1}^{k} \omega_j y_j / \sum_{j=1}^{k} \omega_j \qquad \text{(Eq. 6)}$$

233     $$1/\varepsilon_s^2 = \sum_{j=1}^{k} 1/\varepsilon_j^2 \qquad \text{(Eq. 7)}$$

234   where y_j is O₃ observation of the jth station, ω_j represents the weighting factor of the jth

235   station, y_s and ε_s are the grid-based O₃ observations and errors (superobservation),

236   respectively.

237

3. Results and Discussion

238

3.1 Surface O₃ by assimilating MEE O₃ observations

239

240   We first investigate the effects of surface O₃ observations on single O₃ tracer

241   assimilations. O₃ at the surface level is formed by precursors mixed in the planetary boundary

242   layer (PBL). Thus, it may not be accurate to assume that the differences between simulated and

243   observed surface O₃ concentrations are completely caused by biased O₃ production and loss at

244   the surface level. Here we adjust O₃ concentrations above the surface level within the PBL

245   when assimilating surface O₃ observations:

246     $$\Delta O_3^n = \Delta O_3^1 \times \gamma^{n-1} \qquad \text{(Eq. 8)}$$

247   where ΔO_3^1 is the adjustment at the surface level calculated with Eq. 3; ΔO_3^n is the adjustment

248   at model level n, which is based on ΔO_3^1 but decays exponentially with the increase in model

249   level, and the decay speed is adjusted by the γ parameter. As shown in Table 1, three

250   assimilation experiments (Exp. #5-#7) were conducted to evaluate the effects of the decay

251   speed: 1) $\gamma = 0$ by assuming that the biased surface O₃ concentrations are completely caused

252   by biased O₃ production and loss at the surface level; 2) $\gamma = 1$ by assuming full mixing of O₃

253   biases within the PBL; and 3) $\gamma = 0.8$ by assuming partial mixing of O₃ biases within the

254   PBL, i.e., the adjustment at the 4th model level is approximately 50% of ΔO_3^1, and the

255   adjustment at the 10th model level (close to the top of PBL) is approximately 10% of ΔO_3^1.

256   As shown in Fig. S2A (see the SI), the assimilated surface MDA8 O_3 concentrations

257   show good agreement by using different γ parameters: 42.3, 41.8 and 42.0 ppb ($\gamma = 0$, 0.8 and

258   1.0) in 2015-2020; there are noticeable discrepancies in the trends of assimilated surface O_3

259   concentrations: 0.80, 1.24 and 1.50 ppb yr^{-1} ($\gamma = 0$, 0.8 and 1.0) in 2015-2020 (Fig. S2B), and

260   the trends obtained by considering the mixing of O_3 biases ($\gamma = 0.8$ and 1.0) match better with

261   MEE O_3 observations (1.77 ppb yr^{-1}). Fig. S3 (see the SI) further demonstrates tropospheric O_3

262   columns by assimilating MEE O_3 observations in 2015-2020. We find good agreement in the

263   assimilated tropospheric O_3 columns by using different γ parameters, i.e., the mean

264   tropospheric O_3 columns are 38.1, 37.9 and 37.9 DU, and the trends of tropospheric O_3 columns

265   are 0.11, 0.17 and 0.21 ppb yr^{-1} ($\gamma = 0$, 0.8 and 1.0). Considering the better agreement in the

266   trends of assimilated surface O_3 concentrations ($\gamma = 0.8$ and 1.0) with observations, we finally

267   decide to set $\gamma = 0.8$ as our main assimilation setting by assuming partial mixing of O_3 biases

268   within the PBL.

269   Fig. 4A1-A5 show the annual and seasonal averages of surface MDA8 O_3 observations

270   from MEE stations in 2015-2020. Fig. 4C1-C5 show the annual and seasonal averages of the a

271   posteriori O_3 concentrations by assimilating the MEE O_3 observations. As shown in Fig. 5, the

272   assimilated O_3 concentrations (blue lines) show good agreement with MEE O_3 observations

273   (red lines): the mean surface MDA8 O_3 in 2015-2020 are 43.2, 41.8 and 42.1 ppb (E. China),

274   42.4, 45.6 and 47.6 ppb (North China Plain), 44.6, 45.0 and 44.9 ppb (Yangtze River Delta),

275   45.1, 43.1 and 43.5 ppb (Central China), 45.7, 37.5 and 36.9 ppb (Sichuan Basin), and 43.2,

276   39.2 and 38.3 ppb (Southern China) in the a priori simulations, a posteriori simulations and

277   MEE observations, respectively. It should be noted that Fig. 5A exhibits broadly good

278   agreement between the a priori and a posteriori O_3 concentrations over E. China except for a

279   larger difference in the summer. However, as shown in Fig. 4D1-D5, the good agreements

280   between the a priori and a posteriori O_3 concentrations are caused by the counterbalance of

281 positive biases (i.e., overestimated surface O_3 in the a priori simulations over southern China)

282 and negative biases (i.e., underestimated surface O_3 in the a priori simulations over northern

283 China). The good agreements in Fig. 5A thus cannot represent good performance in the

284 simulations of surface O_3 concentrations.

285   The assimilations exhibit noticeable declines in surface O_3 concentrations over regions

286 #2-5 in June-July, and the declines are underestimated by the a priori simulations (Fig. 5C-F).

287 The inaccurate simulation in June-July thus results in overestimated surface O_3 concentrations

288 in the summer. There is dramatic seasonality in surface O_3 concentrations (Fig. 5): maximum

289 in June in the North China Plain, May and August in the Yangtze River Delta, Central China

290 and Sichuan Basin, and September-October in Southern China. Fig. 4E1-E5 exhibits the effects

291 of seasonal variabilities in background O_3 (Exp. #3) by fixing background O_3 in the spring in

292 the simulations. The fixed background O_3 has limited influences on surface O_3 concentrations,

293 and consequently, the seasonality in surface O_3 concentrations is dominated by local

294 contributions. As we expected, MDA8 O_3 concentrations are higher over areas with higher

295 anthropogenic NO_x emissions, for example, 45.6 and 45.0 ppb in the North China Plain and

296 Yangtze River Delta, respectively, in contrast to 43.1, 37.5 and 39.2 ppb in Central China,

297 Sichuan Basin and Southern China. The influences of regional transport on surface O_3

298 concentrations are limited; for example, O_3 generated within the North China Plain PBL by

299 setting O_3 formation rates within the North China Plain PBL to zero (Exp. #4) are mainly

300 contained within the North China Plain (Fig. 4F1-F5).

301 **3.2 Rapid increasing trends in surface O_3 concentrations**

302   Here we investigate the changes in surface O_3 concentrations from observations and

303 assimilations. As shown in Fig. 6B1-B5, the a priori simulation suggests slightly increasing

304 trends of MDA8 O_3 in 2015-2020: 0.31 (spring), -0.12 (summer), 0.45 (autumn) and 0.40

305 (winter) ppb yr^{-1}, and the relative increasing trends are 0.7 (spring), -0.2 (summer), 1.1

306 (autumn) and 1.4 (winter) % yr^{-1}. The a priori simulation suggests increasing trends of surface

307 O_3 concentrations in the summer over areas with higher local pollution levels, for example,

308 0.68 and 0.63 ppb yr^{-1} over the North China Plain and Yangtze River Delta, respectively, and

309 decreasing trends of surface O_3 concentrations in the summer over areas with lower local

310 pollution levels, for example, -0.83 and -1.01 ppb yr^{-1} over the Sichuan Basin and Southern

311 China, respectively. The decreasing trends over areas with lower local pollution levels in the

312 simulations are not surprising, given the decreases in anthropogenic NO_x emissions (Zheng et

313 al., 2018; Jiang et al., 2022) and the reported NO_x-limited O_3 nonlinear chemical regimes in

314 model simulations (Chen et al., 2021; Liu et al., 2021). Furthermore, as shown in Fig. 6D1-D5,

315 the interannual variabilities in background O_3 (Exp. #2) are suggested to result in increases in

316 surface O_3 concentrations in the a priori simulations in 2015-2020 by 0.02 (spring), 0.05

317 (summer), 0.02 (autumn) and 0.00 (winter) ppb yr^{-1}, and the relative contribution is particularly

318 pronounced in the summer.

319   In contrast, the increasing trends in surface O_3 are much stronger in the assimilations. As

320 shown in Table 2.1, our assimilation suggests 1.60 (spring), 1.16 (summer), 1.47 (autumn) and

321 0.80 (winter) ppb yr^{-1} increases in surface O_3 over E. China in 2015-2020, and the relative

322 increasing trends are 3.4 (spring), 2.2 (summer), 3.7 (autumn) and 2.7 (winter) % yr^{-1}. The

323 annual increasing trend (1.24 ppb yr^{-1}) in the assimilated surface O_3 concentrations is more

324 consistent with the MEE O_3 observations (1.77 ppb yr^{-1}) which are comparable with the

325 reported recent trends in surface O_3 concentrations in China of 1.25-2.0 ppb yr^{-1}

326 (Mousavinezhad et al., 2021; Wei et al., 2022; Wang, W. et al., 2022). The increasing trends

327 are weaker when the modeled surface O_3 concentrations are averaged over E. China (Table

328 2.2) instead of sampling at the locations and times of MEE observations: 0.71 (spring), 0.36

329 (summer), 0.69 (autumn) and 0.54 (winter) ppb yr^{-1} because most MEE stations are urban sites.

330 Our analysis thus indicates a noticeable underestimation in the increasing trends of surface O_3

331 concentrations in China in the a priori simulations, particularly in the summer, despite the

332 anthropogenic NO_x and VOC emissions having been scaled in the simulations following Jiang

333 et al. (2022).

334   The changes in surface O_3 concentrations have significant regional and seasonal

335 discrepancies. As shown in Tables S1-S5 (see the SI), our assimilations demonstrate strong

336 increasing trends in surface O_3 concentrations in 2015-2020 in spring (1.94 ppb yr^{-1} or 3.8%

337 yr^{-1}) and summer (2.52 ppb yr^{-1} or 4.0% yr^{-1}) over the North China Plain; in spring (2.21 ppb

338 yr^{-1} or 4.4% yr^{-1}) and autumn (1.84 ppb yr^{-1} or 4.1% yr^{-1}) over the Yangtze River Delta; in

339 spring (2.07 ppb yr^{-1} or 4.3% yr^{-1}) and autumn (2.09 ppb yr^{-1} or 4.7% yr^{-1}) over Central China;

340 in spring (1.69 ppb yr^{-1} or 3.8% yr^{-1}) over the Sichuan Basin; and in autumn (2.21 ppb yr^{-1} or

341 4.9% yr^{-1}) over Southern China. While surface O_3 concentrations are higher over areas with

342 higher anthropogenic NO_x emissions, the increasing trends in surface O_3 concentrations over

343 Central China and Southern China are comparable with those in the North China Plain and

344 Yangtze River Delta. Our analysis advises more attention to O_3 pollution in spring and autumn

345 over areas with lower anthropogenic NO_x emissions because of the rapid increases in surface

346 O_3 concentrations.

347 **3.3 Tropospheric O_3 columns by assimilating OMI O_3 observations**

348   Fig. 7A1-A5 show the annual and seasonal averages of tropospheric OMI O_3 columns in

349 2015-2020. OMI is sensitive to O_3 at different vertical levels (Huang et al., 2017; Fu et al.,

350 2018), and thus, the standard KF algorithm (Eq. 3) was employed to adjust tropospheric O_3

351 vertical profiles with the application of OMI O_3 averaging kernels. Fig. 7C1-C5 show the

352 annual and seasonal averages of the a posteriori tropospheric O_3 columns by assimilating OMI

353 O_3 observations. The assimilated tropospheric O_3 columns show good agreement with OMI O_3

354 observations: the mean tropospheric O_3 columns in 2015-2020 (Table 2.3) are 37.1 DU in the

355 a priori simulations and 37.9 and 38.0 DU in the a posteriori simulation and OMI observations,

356 respectively. The discrepancies between the a priori and a posteriori simulations in tropospheric

357 O_3 columns (Fig. 7) are smaller than those in surface O_3 concentrations (Fig. 4). A better

358 simulation capability in tropospheric column O_3 is expected because model simulation with

359 $0.5° \times 0.625°$ horizontal resolution may not be enough to accurately resolve O_3 nonlinear

360 chemical regimes over urban surface stations.

361 The above assimilated tropospheric O_3 columns (Exp. #8) are driven by optimized O_3

362 background conditions provided by global assimilations of OMI O_3 as well as row-isolated

363 OMI data by using across-track positions between 4-11. Fig. 7E1-E5 exhibits the effects of

364 optimization on regional O_3 background conditions. The mean assimilated tropospheric O_3

365 column driven by the original O_3 background conditions is 37.6 DU (Exp. #9), which is slightly

366 lower than the 37.9 DU in the main assimilation (Exp. #8). The usage of original O_3 background

367 conditions can result in overestimations over southern China in the spring and winter, and

368 underestimations over northern China in the spring and summer (Fig. 7E1-E5). Fig. 7F1-F5

369 further exhibits the effects of the usage of row-isolated data. The mean assimilated tropospheric

370 O_3 column by assimilating OMI O_3 observations at across-track positions 4-27 is 37.7 DU (Exp.

371 #10), which is slightly lower than the 37.9 DU in the main assimilation (Exp. #8). The

372 underestimations in the assimilated tropospheric O_3 columns are particularly significant in the

373 spring and summer (Fig. 7F2-F3).

374 As shown in Fig. 8, the trends of tropospheric O_3 columns in 2015-2020 (Table 2.3) are

375 0.02 DU yr^{-1} in the a priori simulations and -0.17 and -0.30 DU yr^{-1} in the a posteriori

376 simulation and OMI observations, respectively. In contrast to the wide distributions of

377 increasing trends of O_3 at the surface level (Fig. 6), both OMI O_3 observations (-0.30 DU yr^{-1})

378 and the OMI-based assimilations (-0.17 DU yr^{-1}) suggest decreasing trends in tropospheric O_3

379 columns over E. Asia in 2015-2020 (Fig. 8). The decreasing trends are stronger in the summer

380 and weaker in the spring. Furthermore, the usage of original O_3 background conditions can

381   result in overestimated trend by approximately 0.08 DU yr^{-1} (Fig. 8D1); and the assimilation

382   of OMI O_3 observations at across-track positions 4-27 can result in a similar overestimated

383   trend, by approximately 0.08 DU yr^{-1} (Fig. 8E1). These discrepancies demonstrate the

384   importance of optimized usages of regional O_3 background conditions and OMI O_3

385   observations in the assimilations.

386   **3.4 Changes in tropospheric O_3 columns**

387   The trends shown in Fig. 8 may not represent the actual tropospheric O_3 changes well

388   because the convolution of OMI O_3 averaging kernels on the output O_3 profiles can affect the

389   weights of the derived tropospheric columns to O_3 at different vertical levels. Consequently,

390   Fig. 9 shows the annual and seasonal averages of tropospheric O_3 columns in which the output

391   O_3 profiles are not convolved with OMI retrieval averaging kernels so that they can better

392   represent the actual atmospheric O_3 state. The assimilated tropospheric O_3 columns are 37.9

393   and 38.8 DU (E. China), 42.9 and 43.7 DU (North China Plain), 47.5 and 48.1 DU (Yangtze

394   River Delta), 47.4 and 48.1 DU (Central China), 43.8 and 44.6 DU (Sichuan Basin), and 39.6

395   and 40.6 DU (Southern China) in 2015-2020 by assimilating MEE and OMI O_3 observations,

396   respectively.

397   In contrast to the higher surface MDA8 O_3 concentrations over areas with higher

398   anthropogenic NO_x emissions, tropospheric O_3 columns over Central China and the Sichuan

399   Basin are even higher than those over the highly polluted North China Plain. In addition,

400   tropospheric O_3 columns obtained by assimilating MEE surface O_3 observations are lower than

401   those obtained by assimilating OMI O_3 observations, and their difference is larger in the

402   summer and smaller in the winter. As shown in Fig. S4 (see the SI), the impacts of different

403   surface and satellite O_3 observations on the assimilated O_3 vertical profiles are limited. The

404   assimilation of MEE surface O_3 observations leads to decreases in O_3 concentrations in the

405   lower troposphere from the surface to 600 hPa levels over the Sichuan Basin and Southern

406   China; the assimilation of OMI O_3 observations leads to enhancement in O_3 concentrations in

407   the middle and upper troposphere over the highly polluted North China Plain.

408   The assimilated tropospheric O_3 columns are maximum in June-July over the highly

409   polluted North China Plain and March-May over other lower polluted regions (Fig. S5, see the

410   SI). Fig. 9E1-E5 exhibit the effects of seasonal variabilities in background O_3 (Exp. #3). The

411   fixed background O_3 in the spring can result in dramatic increases in tropospheric O_3 columns

412   by 14.3 (summer), 15.1 (autumn) and 4.8 (winter) DU over E. China. Fig. 9F1-F5 further

413   exhibit the effects of O_3 formation within the North China Plain PBL (Exp. #4) on tropospheric

414   O_3 columns, which are 5.4 (spring), 8.1 (summer), 3.6 (autumn) and 1.3 (winter) DU over the

415   North China Plain. In addition, as shown in Fig. S6 (see the SI), there is a larger enhancement

416   in O_3 production rates in the free troposphere (600-300 hPa) over the North China Plain in the

417   summer than in other lower polluted regions. Consequently, the spring maximum in

418   tropospheric O_3 columns over lower polluted regions is caused by the enhanced background O_3

419   (Fig. 9E1-E5), and the summer maximum in tropospheric O_3 columns over the highly polluted

420   North China Plain is caused by the local contributions from enhanced O_3 formation within the

421   North China Plain PBL (Fig. 9F1-F5) and free troposphere (Fig. S6).

422   As shown in Fig. 10A1-A5, the trends of tropospheric O_3 columns in the a priori

423   simulations in 2015-2020 are -0.02 (spring), 0.02 (summer), 0.29 (autumn) and 0.09 (winter)

424   DU yr^{-1} over E. China. The interannual variability in background O_3 (Fig. 10D1-D5, Exp. #2)

425   is suggested to have important contributions to the trends of tropospheric O_3 columns by 0.09

426   (spring), -0.11 (summer), -0.10 (autumn) and -0.08 (winter) DU yr^{-1}. The trends of assimilated

427   tropospheric O_3 columns are 0.17 and -0.10 DU yr^{-1} (E. China), which are comparable with the

428   reported recent trend in free tropospheric O_3 concentrations over China by -0.14 DU yr^{-1}

429   (Dufour et al., 2021), and are 0.47 and 0.12 DU yr^{-1} (North China Plain), 0.45 and 0.13 DU yr^{-}

430   ^{1} (Yangtze River Delta), 0.32 and -0.06 DU yr^{-1} (Central China), 0.03 and -0.29 DU yr^{-1}

431 (Sichuan Basin), and 0.06 and -0.25 DU yr^{-1} (Southern China) by assimilating MEE and OMI

432 O$_3$ observations, respectively.

433   The stronger increasing trends in tropospheric O$_3$ columns over the highly polluted North

434 China Plain (Fig. 10A1) are suggested to be caused by larger local contributions because of

435 relatively uniform influences from interannual variability in background O$_3$ (Fig. 10D1).

436 Higher positive trends by assimilating MEE observations are expected, given the increasing

437 trends in surface O$_3$ concentrations (1.77 ppb yr^{-1}) and decreasing trends in OMI O$_3$

438 concentrations (-0.30 DU yr^{-1}) over E. China. Furthermore, it should be noted that while the

439 Yangtze River Delta is defined as a highly polluted region in our analysis, its area is much

440 smaller than that of the North China Plain (Fig. 1); thus, the impact of local contributions on

441 tropospheric O$_3$ columns over the Yangtze River Delta is not as strong as that over the North

442 China Plain.

443 **4. Conclusion**

444   A single O$_3$ tracer (tagged-O$_3$) mode was developed in this work to build the capability

445 of the GEOS-Chem model for rapid simulations of tropospheric O$_3$. The single O$_3$ tracer

446 simulation demonstrates consistency with the GEOS-Chem full chemistry simulation. In

447 contrast, the O$_x$ concentrations provided by the tagged-O$_x$ mode are higher than the O$_3$

448 concentrations by approximately 6 ppb, and the relative difference can reach 40% in the winter,

449 which is thus not suitable for direct comparison with observed O$_3$. The computational costs of

450 the single O$_3$ tracer mode are reduced by approximately 91-94% with respect to the full

451 chemistry mode. For example, the computational costs (hours of wall time per simulation year)

452 are 57.5 and 5.2 hours at the global scale (4°×5°) and 80.2 and 4.5 hours within the nested

453 China domain (0.5°×0.625°) by full chemistry and single O$_3$ tracer simulations, respectively.

454 The low computational costs allow us to design and perform different experiments much more

455 efficiently. As shown in Table 1, 10 different simulation and assimilation experiments are

456   performed in this work to analyze the impacts of background and local contributions to surface

457   and free tropospheric O_3 changes over E. China in 2015-2020, which requires 4812 hours (wall

458   time) with the full chemistry simulation but only 270 hours (wall time) with the single O_3 tracer

459   simulation.

460   As an application of the single O_3 tracer mode, the assimilated surface O_3 concentrations

461   demonstrate good agreement with surface O_3 observations: 43.2, 41.8 and 42.1 ppb over E.

462   China in a priori and a posteriori simulations and observations, respectively. We find noticeable

463   biases in modeled surface O_3 concentrations, for example, overestimated surface O_3 over

464   southern China and underestimated surface O_3 over northern China. The assimilations indicate

465   rapidly increasing trends in surface O_3 concentrations by 1.60 (spring), 1.16 (summer), 1.47

466   (autumn) and 0.80 (winter) ppb yr^{-1} over E. China in 2015-2020, and the increasing trends are

467   underestimated by the a priori simulations. While surface O_3 concentrations are higher over

468   areas with higher anthropogenic NO_x emissions, the increasing trends in surface O_3

469   concentrations over Central China and Southern China are comparable with those in the North

470   China Plain and Yangtze River Delta. Our analysis thus advises more attention to O_3 pollution

471   in spring and autumn over areas with lower anthropogenic NO_x emissions in China because of

472   the rapid increases in surface O_3 concentrations.

473   Similarly, the assimilated tropospheric O_3 columns demonstrate good agreement with

474   OMI observations: 37.1, 37.9 and 38.0 DU over E. China in a priori and a posteriori simulations

475   (convolved with OMI retrieval averaging kernels) and OMI observations, respectively. The

476   trends of assimilated tropospheric O_3 columns in 2015-2020 over E. China are 0.09 and -0.17

477   (spring), 0.17 and -0.22 (summer), 0.38 and 0.04 (autumn), and 0.12 and -0.02 (winter) by

478   assimilating MEE and OMI O_3 observations, respectively. We find stronger increasing trends

479   in tropospheric O_3 columns over highly polluted areas due to the larger local contributions, for

480   example, 0.47 and 0.12 DU yr^{-1} (North China Plain) in contrast to 0.03 and -0.29 DU yr^{-1}

481 (Sichuan Basin) and 0.06 and -0.25 DU yr^{-1} (Southern China) by assimilating MEE and OMI

482 O$_3$ observations, respectively. The large discrepancy by assimilating surface and satellite

483 observations indicates the possible uncertainties in the derived free tropospheric O$_3$ changes.

484 The usage of optimized O$_3$ background conditions and row-isolated OMI data is important to

485 produce more reliable results, for example, the usage of original O$_3$ background conditions can

486 result in an overestimated trend by approximately 0.08 DU yr^{-1} in 2015-2020.

487 Our analysis demonstrates noticeable contributions of the interannual variability in

488 background O$_3$ to the trends in tropospheric O$_3$ over E. China. The seasonality in surface O$_3$

489 concentrations is dominated by local contributions; however, the interannual variabilities in

490 background O$_3$ have noticeable contributions to the increasing trends in surface O$_3$ particularly

491 in the summer in the a priori simulations. Moreover, the spring maximum in tropospheric O$_3$

492 columns over lower polluted regions is caused by the enhanced background O$_3$, and the summer

493 maximum in tropospheric O$_3$ columns over the highly polluted North China Plain is caused by

494 enhanced local O$_3$ formation. The interannual variabilities in background O$_3$ have important

495 contributions to the trends in tropospheric O$_3$ columns; for example, the trends of tropospheric

496 O$_3$ columns in 2015-2020 are -0.02 (spring), 0.02 (summer), 0.29 (autumn) and 0.09 (winter)

497 DU yr^{-1} over E. China, and the contributions from interannual variability in background O$_3$ are

498 0.09 (spring), -0.11 (summer), -0.10 (autumn) and -0.08 (winter) DU yr^{-1} in the a priori

499 simulations. Our analysis thus suggests more attention to the impact of background O$_3$ to

500 tropospheric O3 changes in China, particularly in the free troposphere.

501 The capability of rapid O$_3$ simulation developed in this work is a useful tool for

502 interpreting atmospheric O$_3$ observations. Assimilations of surface and satellite observations,

503 as shown in this work, can provide useful information to better describe the changes in surface

504 and free tropospheric O$_3$. Despite these advantages, it should be noted that the linear chemistry

505 assumption by reading the archived PO$_3$ and LO$_3$ implies single O$_3$ tracer mode is good for

506 representing near-current O_3 chemical conditions, particularly, for scientific issues associated

507 with the sources and transport of tropospheric O_3 as well as assimilations in this work and the

508 companion paper (Zhu et al., 2023). More cautious applications are suggested under

509 substantially different O_3 chemical conditions as the linear chemistry assumption could not be

510 satisfied.

511

512 **Code and data availability:** The MEE O_3 data can be downloaded from

513 https://quotsoft.net/air/. The AQS and AirBase surface O_3 data can be downloaded from

514 https://www.eea.europa.eu/data-and-maps/data/aqereporting-8 and

515 https://aqs.epa.gov/aqsweb/airdata/download_files.html#Row. The OMI PROFOZ product

516 can be acquired at

517 https://avdc.gsfc.nasa.gov/pub/data/satellite/Aura/OMI/V03/L2/OMPROFOZ/. The GEOS-

518 Chem model (version 12.8.1) can be downloaded from http://wiki.seas.harvard.edu/geos-

519 chem/index.php/GEOS-Chem_12#12.8.1. The KPP module for tagged-O_3 simulations can be

520 downloaded from https://doi.org/10.5281/zenodo.7545944.

521

522 **Author Contributions**: Z.J. designed the research. R.Z. developed the model code and

523 performed the research. Z.J. and R.Z. wrote the manuscript. X.L. provided instruction for the

524 usage of OMI data. All authors contributed to discussions and editing the manuscript.

525

526 **Competing interests**: The contact author has declared that neither they nor their co-authors

527 have any competing interests.

528

529 **Acknowledgments:** We thank the China Ministry of Ecology and Environment (MEE), the

530 United States Environmental Protection Agency and the European Environmental Agency for

531 providing the surface O_3 measurements. The numerical calculations in this paper have been

532   done on the supercomputing system in the Supercomputing Center of University of Science

533   and Technology of China. This work was supported by the Hundred Talents Program of

534   Chinese Academy of Science and National Natural Science Foundation of China (42277082,

535   41721002).

Table and Figures

537   **Table 1.** Single O_3 tracer simulation and assimilation experiments (Exp.) conducted in this

538   work. Exp. #1: the main a priori simulation; Exp. #2: O_3 boundary conditions and stratospheric

539   O_3 concentrations are fixed in 2015; Exp. #3: O_3 boundary conditions and stratospheric O_3

540   concentrations are fixed in the spring; Exp. #4: O_3 formation rates within the North China Plain

541   PBL are set to zero; Exp. #5: the main assimilation by assimilating MEE surface O_3

542   observations with $\gamma = 0.8$; Exp. #6: only surface O_3 concentrations are adjusted ($\gamma = 0$); Exp.

543   #7: full mixing of O_3 biases within the PBL ($\gamma = 1.0$); Exp. #8: the main assimilation by

544   assimilating OMI O_3 observations; Exp. #9: O_3 boundary conditions are not optimized; Exp.

545   #10: assimilating OMI O_3 observations at across-track positions 4-27.

546

547   **Table 2.** Averages (with units ppb or DU) and trends (with units ppb yr^{-1} or DU yr^{-1}) of surface

548   and tropospheric column O_3 concentrations in 2015-2020 over E. China from observations

549   (MEE and OMI) and a priori (Exp. #1) and a posteriori (KF) simulations (Exp. #5 and #8). The

550   domain definition of E. China is shown by Fig. 1A. T2.1): the modeled surface O_3 is sampled

551   at the locations and times of MEE surface O_3 observations; T2.2): the modeled surface O_3 is

552   averaged over E. China (land only); T2.3): the output O_3 profiles from the a priori and a

553   posteriori simulations are convolved with OMI O_3 averaging kernels; T2.4): the output O_3

554   profiles are NOT convolved with OMI O_3 averaging kernels. The uncertainties in the averages

555   are calculated using the bootstrapping method. The trends and uncertainties in the trends are

556   calculated using the linear fitting of averages by using the least squares method (see details in

557   the SI).

558

559   **Fig. 1.** (A) Anthropogenic NO_x emissions over E. China in 2015; (B) Region definitions for

560   the North China Plain (#1), Yangtze River Delta (#2), Central China (#3), Sichuan Basin (#4)

561   and Southern China (#5). The different colors (red, gray and green) represent grids with high

562   (highest 15%), medium (15-50%) and low (lowest 50%) anthropogenic NO_x emissions.

563   Regions #1 and #2 are defined as highly polluted (HP) regions by excluding grids with low and
564   medium anthropogenic NO_x emissions.

566   **Fig. 2.** Surface MDA8 O_3 in 2015-2020 (annual and seasonal averages) simulated by GEOS-
567   Chem model with (A1-A5) full chemistry mode; (B1-B5) single O_3 tracer (tagged-O_3) mode;
568   and (C1-C5) tagged-O_x mode. The 8-hour range of surface O_x is selected according to the time
569   range of MDA8 O_3.

571   **Fig. 3.** (A) Daily averages of surface MDA8 O_3 over E. China in 2015-2020 from GEOS-Chem
572   full chemistry (black), single O_3 tracer (tagged-O_3) (blue) and tagged-O_x (red) simulations; (B)
573   Monthly averages of MDA8 O_3. The dashed lines in panel B are annual averages.

575   **Fig. 4.** Surface MDA8 O_3 in 2015-2020 (annual and seasonal averages) from (A1-A5) MEE
576   stations; (B1-B5) GEOS-Chem a priori simulation (Exp. #1); (C1-C5) GEOS-Chem a
577   posteriori simulation by assimilating MEE O_3 observations (Exp. #5); (D1-D5) Bias in the a
578   priori simulations (Exp. #1 minus #5). (E1-E5) Effects of seasonal variabilities in background
579   O_3 (Exp. #3 minus #1); (F1-F5) Effects of O_3 formation within the North China Plain PBL
580   (Exp. #1 minus #4).

582   **Fig. 5.** (A-F) Daily averages of surface MDA8 O_3 in 2015-2020 from MEE stations (red) and
583   GEOS-Chem a priori (black, Exp. #1) and a posteriori (blue, Exp. #5) simulations by
584   assimilating MEE O_3 observations. (G-L) Monthly averages of MDA8 O_3. The dashed lines in
585   panels G-L are annual averages. The domain definition of E. China is shown by Fig. 1A.

587   **Fig. 6.** Trends of surface MDA8 O_3 in 2015-2020 (annual and seasonal averages) from (A1-
588   A5) MEE stations; (B1-B5) GEOS-Chem a priori simulation (Exp. #1); (C1-C5) GEOS-Chem
589   a posteriori simulation by assimilating MEE O_3 observations (Exp. #5). (D1-D5) Effects of
590   interannual variabilities in background O_3 (Exp. #1 minus #2).

592   **Fig. 7.** Tropospheric O_3 columns in 2015-2020 (annual and seasonal averages) from (A1-A5)
593   OMI observations; (B1-B5) GEOS-Chem a priori simulation (Exp. #1); (C1-C5) GEOS-Chem
594   a posteriori simulation by assimilating OMI O_3 observations (Exp. #8). (D1-D5) Bias in the a
595   priori simulations (Exp. #1 minus #8). (E1-E5) Effects of optimization on regional O_3

596   background conditions (Exp. #9 minus #8); (F1-F5) Effects of the usage of row-isolated data

597   (Exp. #10 minus #8). The output O_3 profiles are convolved with OMI averaging kernels.

598

599   **Fig. 8.** Trends of tropospheric O_3 columns in 2015-2020 (annual and seasonal averages) from

600   (A1-A5) OMI observations; (B1-B5) GEOS-Chem a priori simulation (Exp. #1); (C1-C5)

601   GEOS-Chem a posteriori simulation by assimilating OMI O_3 observations (Exp. #8). (D1-D5)

602   Effects of optimization on regional O_3 background conditions (Exp. #9 minus #8); (E1-E5)

603   Effects of the usage of row-isolated data (Exp. #10 minus #8). The output O_3 profiles are

604   convolved with OMI averaging kernels.

605

606   **Fig. 9.** Tropospheric O_3 columns in 2015-2020 (annual and seasonal averages) from (A1-A5)

607   GEOS-Chem a priori simulation (Exp. #1); (B1-B5) Assimilations of MEE surface O_3

608   observations (Exp. #5); (C1-C5) Assimilations of OMI O_3 observations (Exp. #8). (D1-D5)

609   Difference in tropospheric O_3 columns calculated by OMI-based assimilations minus MEE-

610   based assimilations (Exp. #8 minus #5). (E1-E5) Effects of seasonal variabilities in background

611   O_3 (Exp. #3 minus #1); (F1-F5) Effects of O_3 formation within the North China Plain PBL

612   (Exp. #1 minus #4). The output O_3 profiles are NOT convolved with OMI averaging kernels.

613

614   **Fig. 10.** Trends of tropospheric O_3 columns in 2015-2020 (annual and seasonal averages) from

615   (A1-A5) GEOS-Chem a priori simulation (Exp. #1); (B1-B5) Assimilations of MEE surface

616   O_3 observations (Exp. #5); (C1-C5) Assimilations of OMI O_3 observations (Exp. #8). (D1-D5)

617   Effects of interannual variabilities in background O_3 (Exp. #1 minus #2). The output O_3 profiles

618   are NOT convolved with OMI averaging kernels.

619

620 **References**

621 Benavides, J., Guevara, M., Snyder, M. G., Rodríguez-Rey, D., Soret, A., Pérez García-Pando,

622   C., and Jorba, O.: On the impact of excess diesel NO_x emissions upon NO_2 pollution in a

623   compact city, Environ Res Let, 16, 10.1088/1748-9326/abd5dd, 2021.

624 Chang, K. L., Guillas, S., and Fioletov, V. E.: Spatial mapping of ground-based observations

625   of total ozone, Atmos Meas Tech, 8, 4487-4505, 10.5194/amt-8-4487-2015, 2015.

626 Chen, J., Jiang, Z., Li, R., Liao, C., Miyazaki, K., and Jones, D. B. A.: Large discrepancy

627   between observed and modeled wintertime tropospheric NO_2 variabilities due to COVID-19

628   controls in China, Environ Res Let, 17, 035007, 10.1088/1748-9326/ac4ec0, 2022.

629 Chen, X., Jiang, Z., Shen, Y., Li, R., Fu, Y., Liu, J., Han, H., Liao, H., Cheng, X., Jones, D. B.

630   A., Worden, H., and Abad, G. G.: Chinese Regulations Are Working—Why Is Surface Ozone

631   Over Industrialized Areas Still High? Applying Lessons From Northeast US Air Quality
632   Evolution, Geophys Res Lett, 48, e2021GL092816, 10.1029/2021gl092816, 2021.

633   Dufour, G., Hauglustaine, D., Zhang, Y., Eremenko, M., Cohen, Y., Gaudel, A., Siour, G.,
634   Lachatre, M., Bense, A., Bessagnet, B., Cuesta, J., Ziemke, J., Thouret, V., and Zheng, B.:
635   Recent ozone trends in the Chinese free troposphere: role of the local emission reductions and
636   meteorology, Atmos Chem Phys, 21, 16001-16025, 10.5194/acp-21-16001-2021, 2021.

637   Elguindi, N., Granier, C., Stavrakou, T., Darras, S., Bauwens, M., Cao, H., Chen, C., Denier
638   van der Gon, H. A. C., Dubovik, O., Fu, T. M., Henze, D. K., Jiang, Z., Keita, S., Kuenen, J.
639   J. P., Kurokawa, J., Liousse, C., Miyazaki, K., Müller, J. F., Qu, Z., Solmon, F., and Zheng,
640   B.: Intercomparison of Magnitudes and Trends in Anthropogenic Surface Emissions From
641   Bottom‐Up Inventories, Top‐Down Estimates, and Emission Scenarios, Earth's Future, 8,
642   e2020EF001520, 10.1029/2020ef001520, 2020.

643   Fu, D., Kulawik, S. S., Miyazaki, K., Bowman, K. W., Worden, J. R., Eldering, A., Livesey,
644   N. J., Teixeira, J., Irion, F. W., Herman, R. L., Osterman, G. B., Liu, X., Levelt, P. F.,
645   Thompson, A. M., and Luo, M.: Retrievals of tropospheric ozone profiles from the synergism
646   of AIRS and OMI: methodology and validation, Atmos Meas Tech, 11, 5587-5605,
647   10.5194/amt-11-5587-2018, 2018.

648   Han, H., Liu, J., Yuan, H., Zhuang, B., Zhu, Y., Wu, Y., Yan, Y., and Ding, A.: Characteristics
649   of intercontinental transport of tropospheric ozone from Africa to Asia, Atmos Chem Phys,
650   18, 4251-4276, 10.5194/acp-18-4251-2018, 2018.

651   Han, W., He, T.-L., Tang, Z., Wang, M., Jones, D., and Jiang, Z.: A comparative analysis for
652   a deep learning model (hyDL-CO v1.0) and Kalman filter to predict CO concentrations in
653   China, Geosci Model Dev, 15, 4225-4237, 10.5194/gmd-15-4225-2022, 2022.

654   Hoesly, R. M., Smith, S. J., Feng, L., Klimont, Z., Janssens-Maenhout, G., Pitkanen, T.,
655   Seibert, J. J., Vu, L., Andres, R. J., Bolt, R. M., Bond, T. C., Dawidowski, L., Kholod, N.,
656   Kurokawa, J.-i., Li, M., Liu, L., Lu, Z., Moura, M. C. P., O'Rourke, P. R., and Zhang, Q.:
657   Historical (1750–2014) anthropogenic emissions of reactive gases and aerosols from the
658   Community Emissions Data System (CEDS), Geosci Model Dev, 11, 369-408, 10.5194/gmd-
659   11-369-2018, 2018.

660   Huang, G., Liu, X., Chance, K., Yang, K., Bhartia, P. K., Cai, Z., Allaart, M., Ancellet, G.,
661   Calpini, B., Coetzee, G. J. R., Cuevas-Agulló, E., Cupeiro, M., De Backer, H., Dubey, M. K.,
662   Fuelberg, H. E., Fujiwara, M., Godin-Beekmann, S., Hall, T. J., Johnson, B., Joseph, E., Kivi,
663   R., Kois, B., Komala, N., König-Langlo, G., Laneve, G., Leblanc, T., Marchand, M.,
664   Minschwaner, K. R., Morris, G., Newchurch, M. J., Ogino, S.-Y., Ohkawara, N., Piters, A. J.
665   M., Posny, F., Querel, R., Scheele, R., Schmidlin, F. J., Schnell, R. C., Schrems, O., Selkirk,
666   H., Shiotani, M., Skrivánková, P., Stübi, R., Taha, G., Tarasick, D. W., Thompson, A. M.,
667   Thouret, V., Tully, M. B., Van Malderen, R., Vömel, H., von der Gathen, P., Witte, J. C., and
668   Yela, M.: Validation of 10-year SAO OMI Ozone Profile (PROFOZ) product using
669   ozonesonde observations, Atmos Meas Tech, 10, 2455-2475, 10.5194/amt-10-2455-2017,
670   2017.

671 Huijnen, V., Miyazaki, K., Flemming, J., Inness, A., Sekiya, T., and Schultz, M. G.: An
672 intercomparison of tropospheric ozone reanalysis products from CAMS, CAMS interim,
673 TCR-1, and TCR-2, Geosci Model Dev, 13, 1513-1544, 10.5194/gmd-13-1513-2020, 2020.
674 Iglesias-Suarez, F., Kinnison, D. E., Rap, A., Maycock, A. C., Wild, O., and Young, P. J.: Key
675 drivers of ozone change and its radiative forcing over the 21st century, Atmos Chem Phys,
676 18, 6121-6139, 10.5194/acp-18-6121-2018, 2018.
677 Jiang, Z., Miyazaki, K., Worden, J. R., Liu, J. J., Jones, D. B. A., and Henze, D. K.: Impacts of
678 anthropogenic and natural sources on free tropospheric ozone over the Middle East, Atmos
679 Chem Phys, 16, 6537-6546, 10.5194/acp-16-6537-2016, 2016.
680 Jiang, Z., Zhu, R., Miyazaki, K., McDonald, B. C., Klimont, Z., Zheng, B., Boersma, K. F.,
681 Zhang, Q., Worden, H., Worden, J. R., Henze, D. K., Jones, D. B. A., Denier van der Gon,
682 H. A. C., and Eskes, H.: Decadal Variabilities in Tropospheric Nitrogen Oxides Over United
683 States, Europe, and China, J Geophys Res-Atmos, 127, e2021JD035872,
684 10.1029/2021jd035872, 2022.
685 Li, D., Shindell, D., Ding, D., Lu, X., Zhang, L., and Zhang, Y.: Surface ozone impacts on
686 major crop production in China from 2010 to 2017, Atmos Chem Phys, 22, 2625-2638,
687 10.5194/acp-22-2625-2022, 2022.
688 Li, K., Jacob, D. J., Liao, H., Shen, L., Zhang, Q., and Bates, K. H.: Anthropogenic drivers of
689 2013-2017 trends in summer surface ozone in China, Proc Natl Acad Sci USA, 116, 422-427,
690 10.1073/pnas.1812168116, 2019.
691 Li, M., Zhang, Q., Kurokawa, J.-i., Woo, J.-H., He, K., Lu, Z., Ohara, T., Song, Y., Streets, D.
692 G., Carmichael, G. R., Cheng, Y., Hong, C., Huo, H., Jiang, X., Kang, S., Liu, F., Su, H., and
693 Zheng, B.: MIX: a mosaic Asian anthropogenic emission inventory under the international
694 collaboration framework of the MICS-Asia and HTAP, Atmos Chem Phys, 17, 935-963,
695 10.5194/acp-17-935-2017, 2017.
696 Li, M., Zhang, Q., Zheng, B., Tong, D., Lei, Y., Liu, F., Hong, C., Kang, S., Yan, L., Zhang,
697 Y., Bo, Y., Su, H., Cheng, Y., and He, K.: Persistent growth of anthropogenic non-methane
698 volatile organic compound (NMVOC) emissions in China during 1990–2017: drivers,
699 speciation and ozone formation potential, Atmos Chem Phys, 19, 8897-8913, 10.5194/acp-
700 19-8897-2019, 2019.
701 Li, R., Zhao, Y., Zhou, W., Meng, Y., Zhang, Z., and Fu, H.: Developing a novel hybrid model
702 for the estimation of surface 8 h ozone (O_3) across the remote Tibetan Plateau during 2005–
703 2018, Atmos Chem Phys, 20, 6159-6175, 10.5194/acp-20-6159-2020, 2020.
704 Liu, X., Bhartia, P. K., Chance, K., Spurr, R. J. D., and Kurosu, T. P.: Ozone profile retrievals
705 from the Ozone Monitoring Instrument, Atmos Chem Phys, 10, 2521-2537, 10.5194/acp-10-
706 2521-2010, 2010.
707 Liu, X., Zhu, Y., Xue, L., Desai, A. R., and Wang, H.: Cluster‐Enhanced Ensemble Learning
708 for Mapping Global Monthly Surface Ozone From 2003 to 2019, Geophys Res Lett, 49,
709 e2022GL097947, 10.1029/2022gl097947, 2022.
710 Liu, Z., Doherty, R. M., Wild, O., Hollaway, M., and O'Connor, F. M.: Contrasting chemical
711 environments in summertime for atmospheric ozone across major Chinese industrial regions:

the effectiveness of emission control strategies, Atmos Chem Phys, 21, 10689-10706, 10.5194/acp-21-10689-2021, 2021.

Logan, J. A., Staehelin, J., Megretskaia, I. A., Cammas, J. P., Thouret, V., Claude, H., De Backer, H., Steinbacher, M., Scheel, H. E., Stübi, R., Fröhlich, M., and Derwent, R.: Changes in ozone over Europe: Analysis of ozone measurements from sondes, regular aircraft (MOZAIC) and alpine surface sites, J Geophys Res-Atmos, 117, n/a-n/a, 10.1029/2011jd016952, 2012.

Ma, C., Wang, T., Mizzi, A. P., Anderson, J. L., Zhuang, B., Xie, M., and Wu, R.: Multiconstituent Data Assimilation With WRF‐Chem/DART: Potential for Adjusting Anthropogenic Emissions and Improving Air Quality Forecasts Over Eastern China, J Geophys Res-Atmos, 7393–7412, 10.1029/2019jd030421, 2019.

Mickley, L. J.: Climate response to the increase in tropospheric ozone since preindustrial times: A comparison between ozone and equivalent CO2forcings, Journal of Geophysical Research, 109, 10.1029/2003jd003653, 2004.

Miyazaki, K., Eskes, H., Sudo, K., Boersma, K. F., Bowman, K., and Kanaya, Y.: Decadal changes in global surface NO_x emissions from multi-constituent satellite data assimilation, Atmos Chem Phys, 17, 807-837, 10.5194/acp-17-807-2017, 2017.

Mousavinezhad, S., Choi, Y., Pouyaei, A., Ghahremanloo, M., and Nelson, D. L.: A comprehensive investigation of surface ozone pollution in China, 2015–2019: Separating the contributions from meteorology and precursor emissions, Atmospheric Research, 257, 10.1016/j.atmosres.2021.105599, 2021.

Oetjen, H., Payne, V. H., Neu, J. L., Kulawik, S. S., Edwards, D. P., Eldering, A., Worden, H. M., and Worden, J. R.: A joint data record of tropospheric ozone from Aura-TES and MetOp-IASI, Atmos Chem Phys, 16, 10229-10239, 10.5194/acp-16-10229-2016, 2016.

Parrington, M., Jones, D. B. A., Bowman, K. W., Horowitz, L. W., Thompson, A. M., Tarasick, D. W., and Witte, J. C.: Estimating the summertime tropospheric ozone distribution over North America through assimilation of observations from the Tropospheric Emission Spectrometer, Journal of Geophysical Research, 113, 10.1029/2007jd009341, 2008.

Parrington, M., Palmer, P. I., Henze, D. K., Tarasick, D. W., Hyer, E. J., Owen, R. C., Helmig, D., Clerbaux, C., Bowman, K. W., Deeter, M. N., Barratt, E. M., Coheur, P. F., Hurtmans, D., Jiang, Z., George, M., and Worden, J. R.: The influence of boreal biomass burning emissions on the distribution of tropospheric ozone over North America and the North Atlantic during 2010, Atmos Chem Phys, 12, 2077-2098, 10.5194/acp-12-2077-2012, 2012.

Parrish, D. D., Derwent, R. G., Turnock, S. T., O'Connor, F. M., Staehelin, J., Bauer, S. E., Deushi, M., Oshima, N., Tsigaridis, K., Wu, T., and Zhang, J.: Investigations on the anthropogenic reversal of the natural ozone gradient between northern and southern midlatitudes, Atmos Chem Phys, 21, 9669-9679, 10.5194/acp-21-9669-2021, 2021.

Peng, X., Shen, H., Zhang, L., Zeng, C., Yang, G., and He, Z.: Spatially continuous mapping of daily global ozone distribution (2004–2014) with the Aura OMI sensor, J Geophys Res-Atmos, 121, 12,702-712,722, 10.1002/2016jd025013, 2016.

Peng, X., Wang, W., Xia, M., Chen, H., Ravishankara, A. R., Li, Q., Saiz-Lopez, A., Liu, P., Zhang, F., Zhang, C., Xue, L., Wang, X., George, C., Wang, J., Mu, Y., Chen, J., and Wang,

T.: An unexpected large continental source of reactive bromine and chlorine with significant impact on wintertime air quality, Natl Sci Rev, 8, nwaa304, 10.1093/nsr/nwaa304, 2021.

Prinn, R. G.: The Cleansing Capacity of the Atmosphere, Annual Review of Environment and Resources, 28, 29-57, 10.1146/annurev.energy.28.011503.163425, 2003.

Schaap, M., Cuvelier, C., Hendriks, C., Bessagnet, B., Baldasano, J. M., Colette, A., Thunis, P., Karam, D., Fagerli, H., Graff, A., Kranenburg, R., Nyiri, A., Pay, M. T., Rouïl, L., Schulz, M., Simpson, D., Stern, R., Terrenoire, E., and Wind, P.: Performance of European chemistry transport models as function of horizontal resolution, Atmos Environ, 112, 90-105, 10.1016/j.atmosenv.2015.04.003, 2015.

Spurr, R. J. D.: VLIDORT: A linearized pseudo-spherical vector discrete ordinate radiative transfer code for forward model and retrieval studies in multilayer multiple scattering media, Journal of Quantitative Spectroscopy and Radiative Transfer, 102, 316-342, 10.1016/j.jqsrt.2006.05.005, 2006.

Tang, Z., Chen, J., and Jiang, Z.: Discrepancy in assimilated atmospheric CO over East Asia in 2015–2020 by assimilating satellite and surface CO measurements, Atmos Chem Phys, 22, 7815-7826, 10.5194/acp-22-7815-2022, 2022.

Thompson, A. M.: The oxidizing capacity of the earth's atmosphere: probable past and future changes, Science, 256, 1157-1165, 10.1126/science.256.5060.1157, 1992.

van der Werf, G. R., Randerson, J. T., Giglio, L., Collatz, G. J., Mu, M., Kasibhatla, P. S., Morton, D. C., DeFries, R. S., Jin, Y., and van Leeuwen, T. T.: Global fire emissions and the contribution of deforestation, savanna, forest, agricultural, and peat fires (1997–2009), Atmos Chem Phys, 10, 11707-11735, 10.5194/acp-10-11707-2010, 2010.

Wang, W., Parrish, D. D., Wang, S., Bao, F., Ni, R., Li, X., Yang, S., Wang, H., Cheng, Y., and Su, H.: Long-term trend of ozone pollution in China during 2014–2020: distinct seasonal and spatial characteristics and ozone sensitivity, Atmos Chem Phys, 22, 8935-8949, 10.5194/acp-22-8935-2022, 2022.

Wang, X., Fu, T. M., Zhang, L., Lu, X., Liu, X., Amnuaylojaroen, T., Latif, M. T., Ma, Y., Zhang, L., Feng, X., Zhu, L., Shen, H., and Yang, X.: Rapidly Changing Emissions Drove Substantial Surface and Tropospheric Ozone Increases Over Southeast Asia, Geophys Res Lett, 49, e2022GL100223, 10.1029/2022gl100223, 2022.

Wei, J., Li, Z., Li, K., Dickerson, R. R., Pinker, R. T., Wang, J., Liu, X., Sun, L., Xue, W., and Cribb, M.: Full-coverage mapping and spatiotemporal variations of ground-level ozone (O_3) pollution from 2013 to 2020 across China, Remote Sens Environ, 270, 10.1016/j.rse.2021.112775, 2022.

Zhang, L., Jacob, D. J., Boersma, K. F., Jaffe, D. A., Olson, J. R., Bowman, K. W., Worden, J. R., Thompson, A. M., Avery, M. A., Cohen, R. C., Dibb, J. E., Flock, F. M., Fuelberg, H. E., Huey, L. G., McMillan, W. W., Singh, H. B., and Weinheimer, A. J.: Transpacific transport of ozone pollution and the effect of recent Asian emission increases on air quality in North America: an integrated analysis using satellite, aircraft, ozonesonde, and surface observations, Atmos Chem Phys, 8, 6117-6136, DOI 10.5194/acp-8-6117-2008, 2008.

Zhang, Y., Shindell, D., Seltzer, K., Shen, L., Lamarque, J.-F., Zhang, Q., Zheng, B., Xing, J., Jiang, Z., and Zhang, L.: Impacts of emission changes in China from 2010 to 2017 on

domestic and intercontinental air quality and health effect, Atmos Chem Phys, 21, 16051-16065, 10.5194/acp-21-16051-2021, 2021.

Zheng, B., Tong, D., Li, M., Liu, F., Hong, C., Geng, G., Li, H., Li, X., Peng, L., Qi, J., Yan, L., Zhang, Y., Zhao, H., Zheng, Y., He, K., and Zhang, Q.: Trends in China's anthropogenic emissions since 2010 as the consequence of clean air actions, Atmos Chem Phys, 18, 14095-14111, 10.5194/acp-18-14095-2018, 2018.

Zhu, R., Tang, Z., Chen, X., Liu, X., and Jiang, Z.: Rapid O_3 assimilations – Part 2: Tropospheric O_3 changes accompanied by declining NO_x emissions in the USA and Europe in 2005–2020, Atmos Chem Phys, 23, 9745-9763, 10.5194/acp-23-9745-2023, 2023.

Zhu, Y., Liu, J., Wang, T., Zhuang, B., Han, H., Wang, H., Chang, Y., and Ding, K.: The Impacts of Meteorology on the Seasonal and Interannual Variabilities of Ozone Transport From North America to East Asia, J Geophys Res-Atmos, 122, 10,612-610,636, 10.1002/2017jd026761, 2017.

Ziemke, J. R., Oman, L. D., Strode, S. A., Douglass, A. R., Olsen, M. A., McPeters, R. D., Bhartia, P. K., Froidevaux, L., Labow, G. J., Witte, J. C., Thompson, A. M., Haffner, D. P., Kramarova, N. A., Frith, S. M., Huang, L.-K., Jaross, G. R., Seftor, C. J., Deland, M. T., and Taylor, S. L.: Trends in global tropospheric ozone inferred from a composite record of TOMS/OMI/MLS/OMPS satellite measurements and the MERRA-2 GMI simulation, Atmos Chem Phys, 19, 3257-3269, 10.5194/acp-19-3257-2019, 2019.

	Experiments	Observations	O3 Boundary Conditions	Other Settings
A priori Simulations	#1 (Main)	N/A	Original (2015-2020)	
	#2	N/A	Original (2015, fixed)	
	#3	N/A	Original (2015-2020, fixed in spring)	
	#4	N/A	Original (2015-2020)	PO3 = 0 (NCP)
Kalman Filter Assimilations	#5 (Main)	MEE	Original (2015-2020)	γ = 0.8
	#6	MEE	Original (2015-2020)	γ = 0.0
	#7	MEE	Original (2015-2020)	γ = 1.0
	#8 (Main)	OMI	Optimized (2015-2020)	positions: 4-11
	#9	OMI	Original (2015-2020)	positions: 4-11
	#10	OMI	Optimized (2015-2020)	positions: 4-27

Table. 1. Single O_3 tracer simulation and assimilation experiments (Exp.) conducted in this work. Exp. #1: the main a priori simulation; Exp. #2: O_3 boundary conditions and stratospheric O_3 concentrations are fixed in 2015; Exp. #3: O_3 boundary conditions and stratospheric O_3 concentrations are fixed in the spring; Exp. #4: O_3 formation rates within the North China Plain PBL are set to zero; Exp. #5: the main assimilation by assimilating MEE surface O_3 observations with $\gamma = 0.8$; Exp. #6: only surface O_3 concentrations are adjusted ($\gamma = 0$); Exp. #7: full mixing of O_3 biases within the PBL ($\gamma = 1.0$); Exp. #8: the main assimilation by assimilating OMI O_3 observations; Exp. #9: O_3 boundary conditions are not optimized; Exp. #10: assimilating OMI O_3 observations at across-track positions 4-27.

E. China (2015-2020)		Annual		Spring		Summer		Autumn		Winter	
		Mean	Trend	Mean	Trend	Mean	Trend	Mean	Trend	Mean	Trend
T2.1 surface (sampled)	MEE	42.1±0.3	1.77±0.38	48.4±0.4	2.25±0.46	51.7±0.6	1.70±0.64	39.8±0.4	2.01±0.60	29.6±0.2	1.14±0.49
	a priori	43.2±0.2	0.21±0.13	48.0±0.2	0.31±0.15	56.3±0.5	-0.12±0.38	40.1±0.3	0.45±0.19	28.5±0.3	0.40±0.17
	KF-MEE	41.8±0.2	1.24±0.28	47.2±0.3	1.60±0.34	51.7±0.5	1.16±0.55	39.5±0.3	1.47±0.47	29.5±0.2	0.80±0.37
T2.2 surface	a priori	42.6±0.1	0.10±0.11	47.7±0.1	0.16±0.11	53.1±0.2	-0.19±0.29	39.1±0.1	0.25±0.19	30.8±0.2	0.35±0.13
	KF-MEE	41.3±0.1	0.55±0.17	46.7±0.1	0.71±0.17	49.8±0.2	0.36±0.36	38.0±0.1	0.69±0.31	31.0±0.2	0.54±0.19
T2.3 trop. column (convolved)	OMI	38.0±0.2	-0.30±0.19	40.9±0.2	0.12±0.20	45.9±0.2	-0.66±0.44	34.6±0.2	-0.41±0.30	30.4±0.2	-0.48±0.40
	a priori	37.1±0.1	0.02±0.14	41.0±0.2	0.17±0.24	43.2±0.2	-0.19±0.16	32.6±0.1	0.15±0.19	31.3±0.2	-0.06±0.18
	KF-OMI	37.9±0.1	-0.17±0.15	41.1±0.2	0.08±0.07	45.5±0.2	-0.51±0.37	34.2±0.1	-0.17±0.24	30.7±0.1	-0.17±0.23
T2.4 trop. Column	a priori	38.3±0.1	0.07±0.14	42.8±0.2	-0.02±0.46	42.5±0.2	0.02±0.16	33.3±0.1	0.29±0.11	34.8±0.2	0.09±0.32
	KF-MEE	37.9±0.1	0.17±0.16	42.6±0.2	0.09±0.47	41.8±0.2	0.17±0.15	33.0±0.1	0.38±0.12	34.7±0.2	0.12±0.32
	KF-OMI	38.8±0.1	-0.10±0.25	42.9±0.2	-0.17±0.57	44.1±0.2	-0.22±0.26	34.4±0.1	0.04±0.12	34.2±0.2	-0.02±0.30

Table. 2. Averages (with units ppb or DU) and trends (with units ppb yr^{-1} or DU yr^{-1}) of surface and tropospheric column O_3 concentrations in 2015-2020 over E. China from observations (MEE and OMI) and a priori (Exp. #1) and a posteriori (KF) simulations (Exp. #5 and #8). The domain definition of E. China is shown by Fig. 1A. T2.1): the modeled surface O_3 is sampled at the locations and times of MEE surface O_3 observations; T2.2): the modeled surface O_3 is averaged over E. China (land only); T2.3): the output O_3 profiles from the a priori and a posteriori simulations are convolved with OMI O_3 averaging kernels; T2.4): the output O_3 profiles are NOT convolved with OMI O_3 averaging kernels. The uncertainties in the averages are calculated using the bootstrapping method. The trends and uncertainties in the trends are calculated using the linear fitting of averages by using the least squares method (see details in the SI).
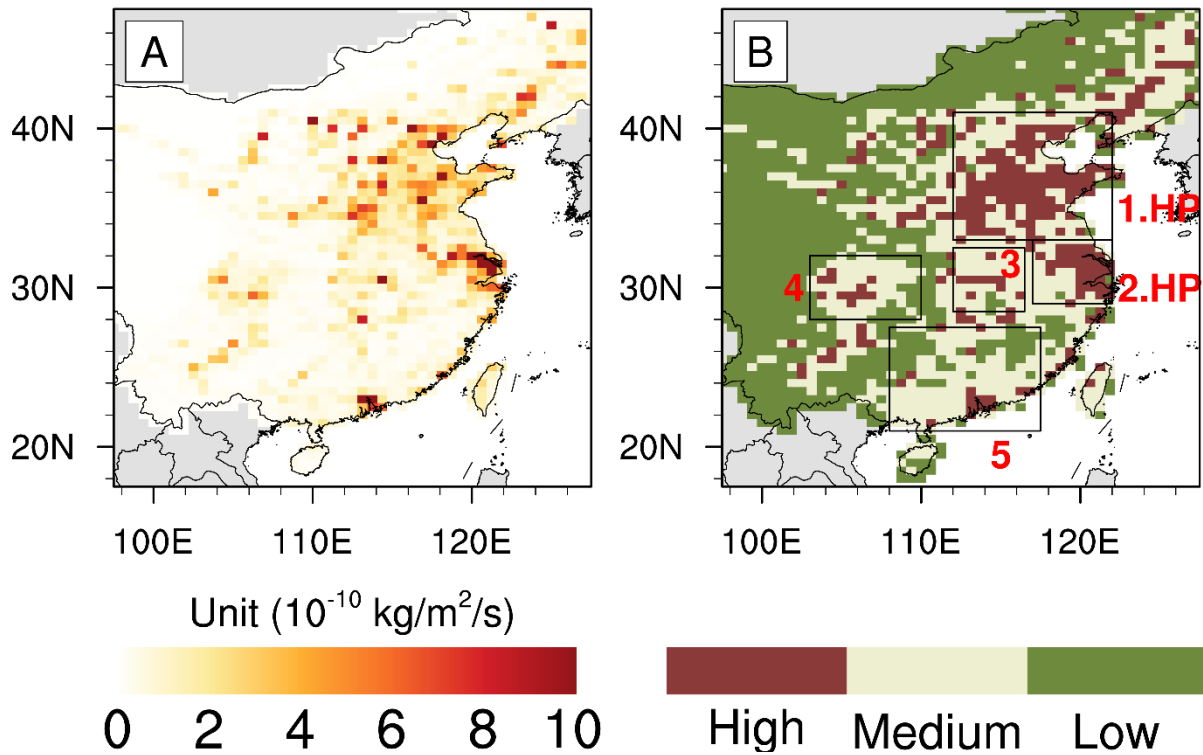
Fig. 1. (A) Anthropogenic NO$_x$ emissions over E. China in 2015; (B) Region definitions for the North China Plain (#1), Yangtze River Delta (#2), Central China (#3), Sichuan Basin (#4) and Southern China (#5). The different colors (red, gray and green) represent grids with high (highest 15%), medium (15-50%) and low (lowest 50%) anthropogenic NO$_x$ emissions. Regions #1 and #2 are defined as highly polluted (HP) regions by excluding grids with low and medium anthropogenic NO$_x$ emissions.
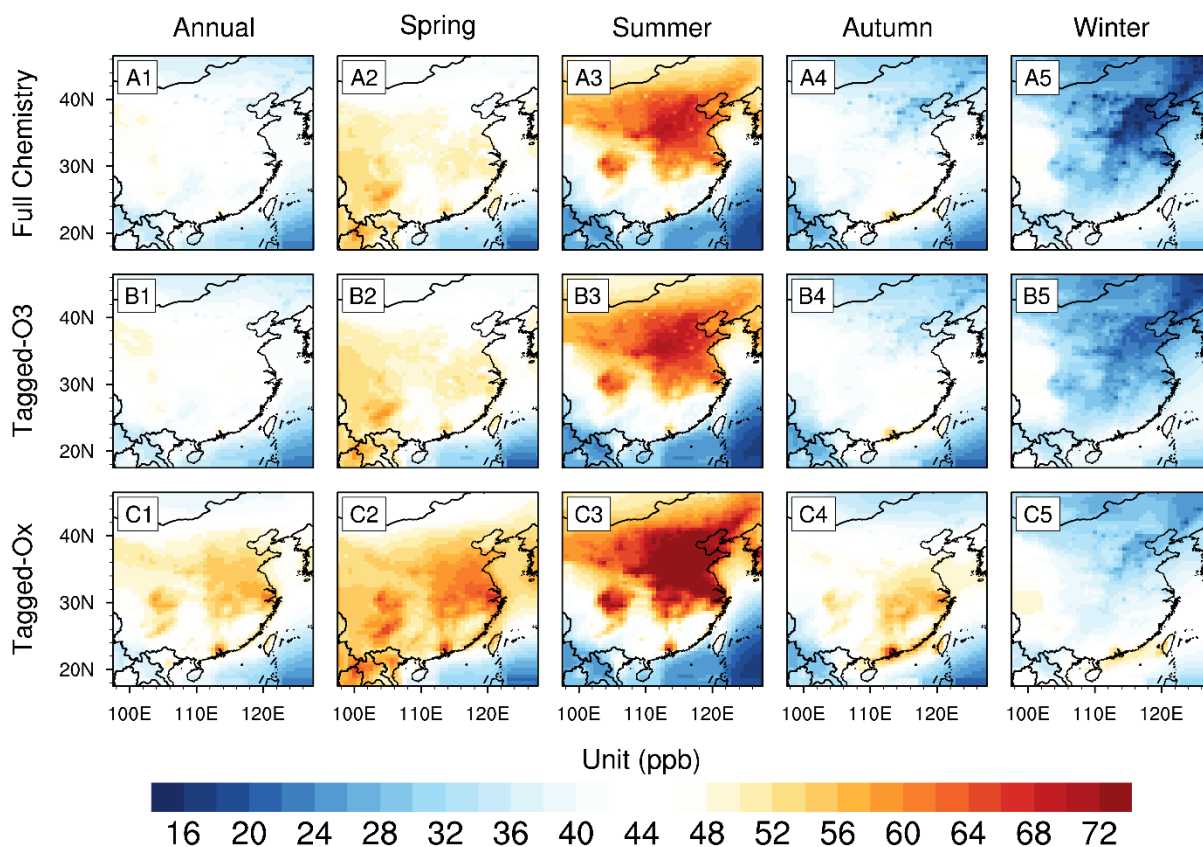
Fig. 2. Surface MDA8 O$_3$ in 2015-2020 (annual and seasonal averages) simulated by GEOS-Chem model with (A1-A5) full chemistry mode; (B1-B5) single O$_3$ tracer (tagged-O$_3$) mode; and (C1-C5) tagged-O$_x$ mode. The 8-hour range of surface O$_x$ is selected according to the time range of MDA8 O$_3$.
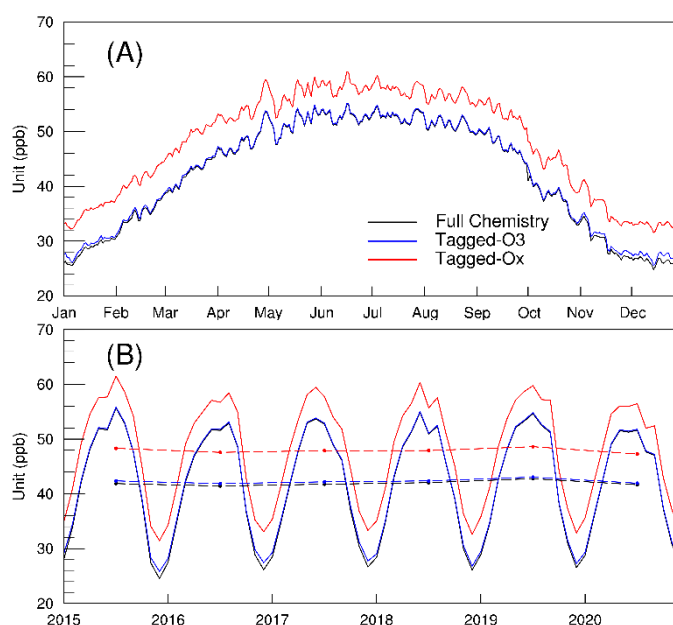
Fig. 3. (A) Daily averages of surface MDA8 O$_3$ over E. China in 2015-2020 from GEOS-Chem full chemistry (black), single O$_3$ tracer (tagged-O$_3$) (blue) and tagged-O$_x$ (red) simulations; (B) Monthly averages of MDA8 O$_3$. The dashed lines in panel B are annual averages.
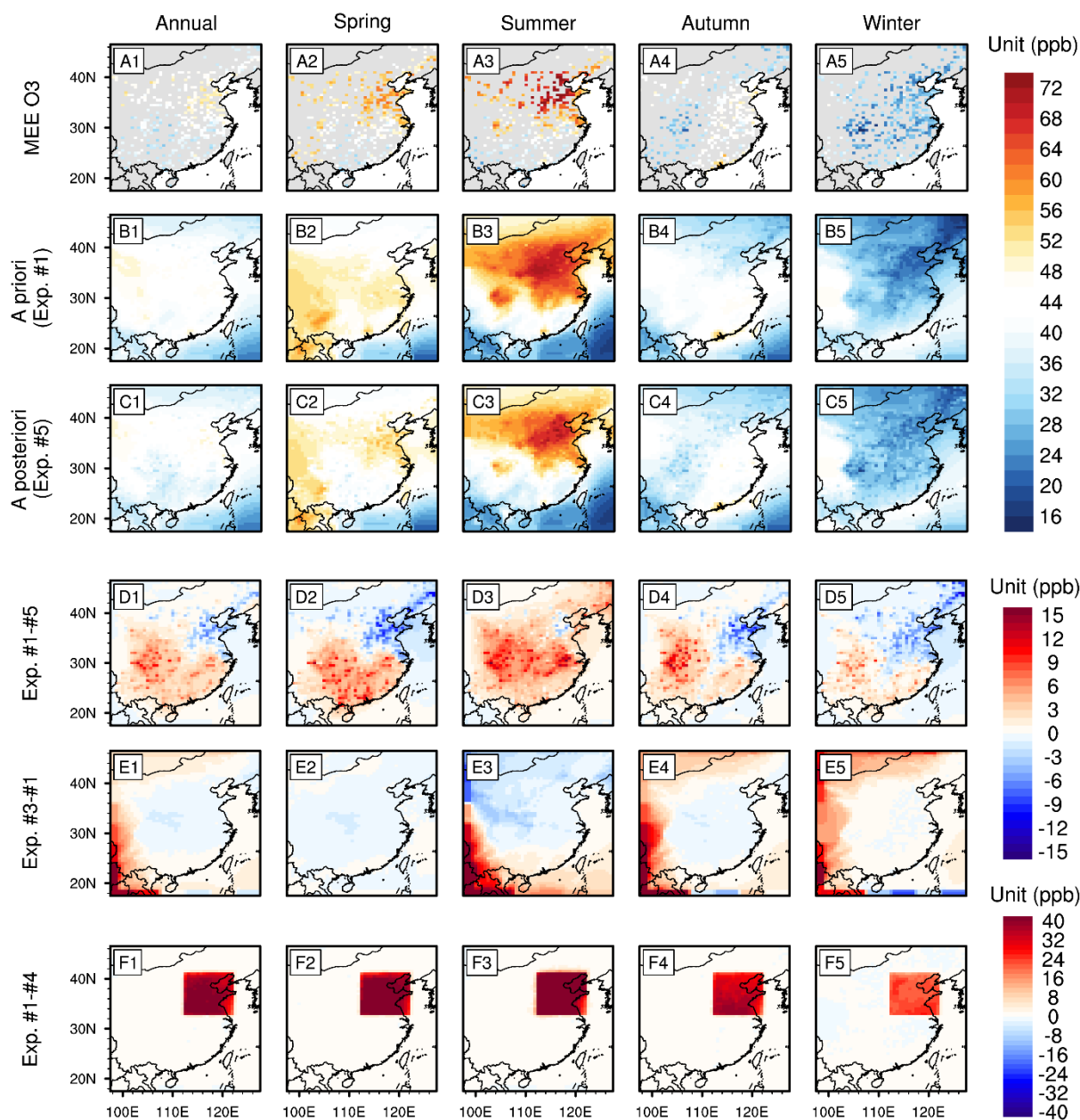
Fig. 4. Surface MDA8 O$_3$ in 2015-2020 (annual and seasonal averages) from (A1-A5) MEE stations; (B1-B5) GEOS-Chem a priori simulation (Exp. #1); (C1-C5) GEOS-Chem a posteriori simulation by assimilating MEE O$_3$ observations (Exp. #5); (D1-D5) Bias in the a priori simulations (Exp. #1 minus #5). (E1-E5) Effects of seasonal variabilities in background O$_3$ (Exp. #3 minus #1); (F1-F5) Effects of O$_3$ formation within the North China Plain PBL (Exp. #1 minus #4).
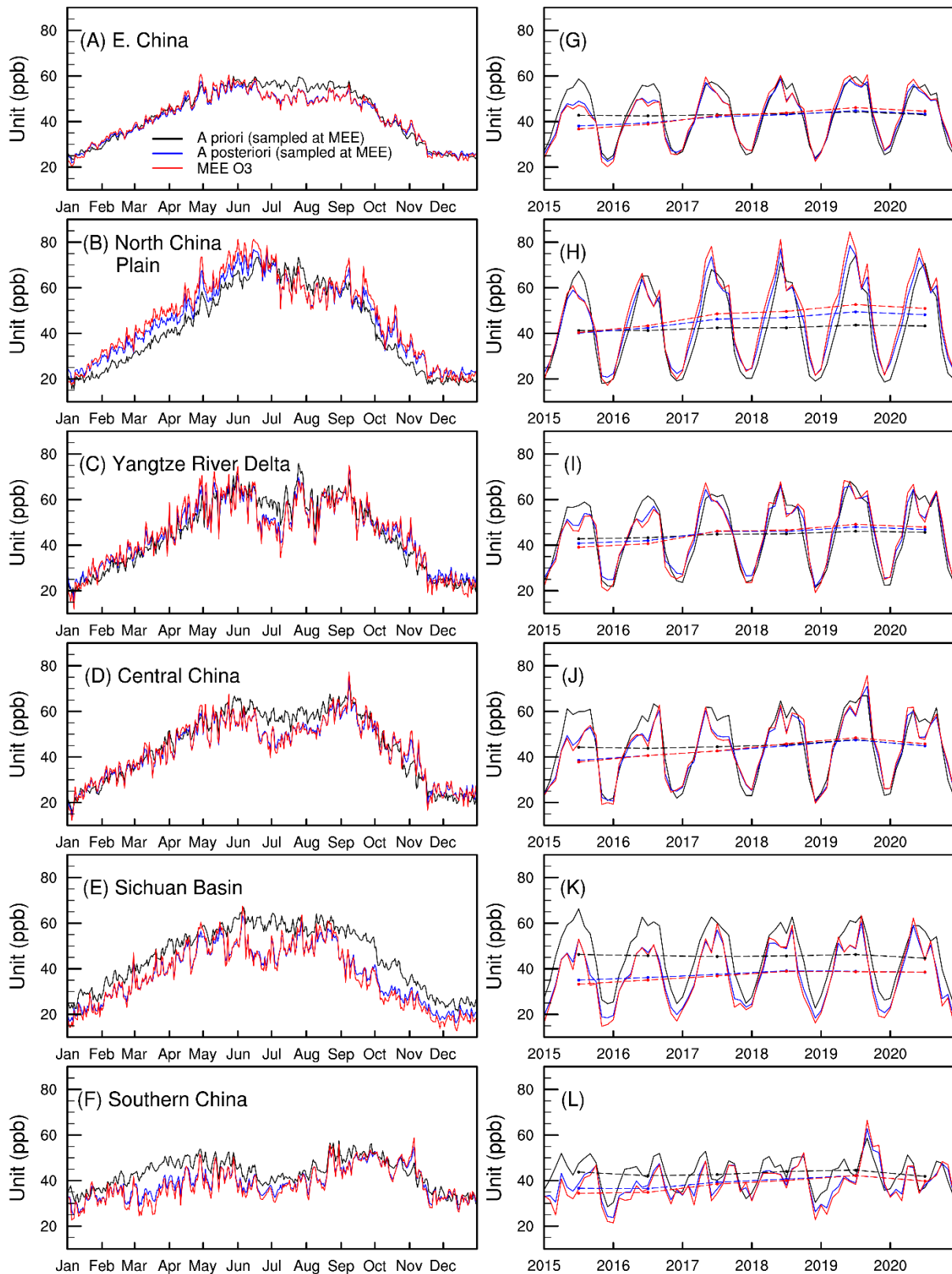
Fig. 5. (A-F) Daily averages of surface MDA8 O₃ in 2015-2020 from MEE stations (red) and GEOS-Chem a priori (black, Exp. #1) and a posteriori (blue, Exp. #5) simulations by assimilating MEE O₃ observations. (G-L) Monthly averages of MDA8 O₃. The dashed lines in panels G-L are annual averages. The domain definition of E. China is shown by Fig. 1A.
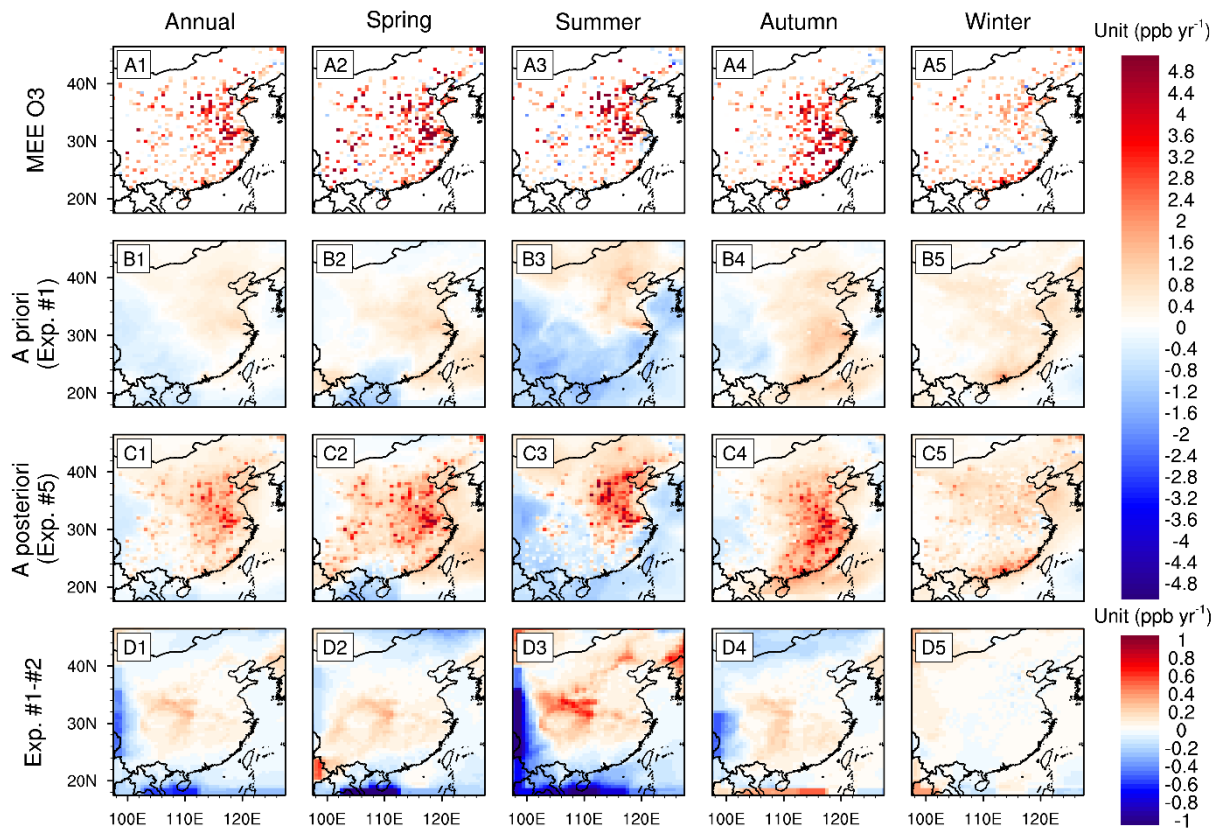
Fig. 6. Trends of surface MDA8 O₃ in 2015-2020 (annual and seasonal averages) from (A1-A5) MEE stations; (B1-B5) GEOS-Chem a priori simulation (Exp. #1); (C1-C5) GEOS-Chem a posteriori simulation by assimilating MEE O₃ observations (Exp. #5). (D1-D5) Effects of interannual variabilities in background O₃ (Exp. #1 minus #2).
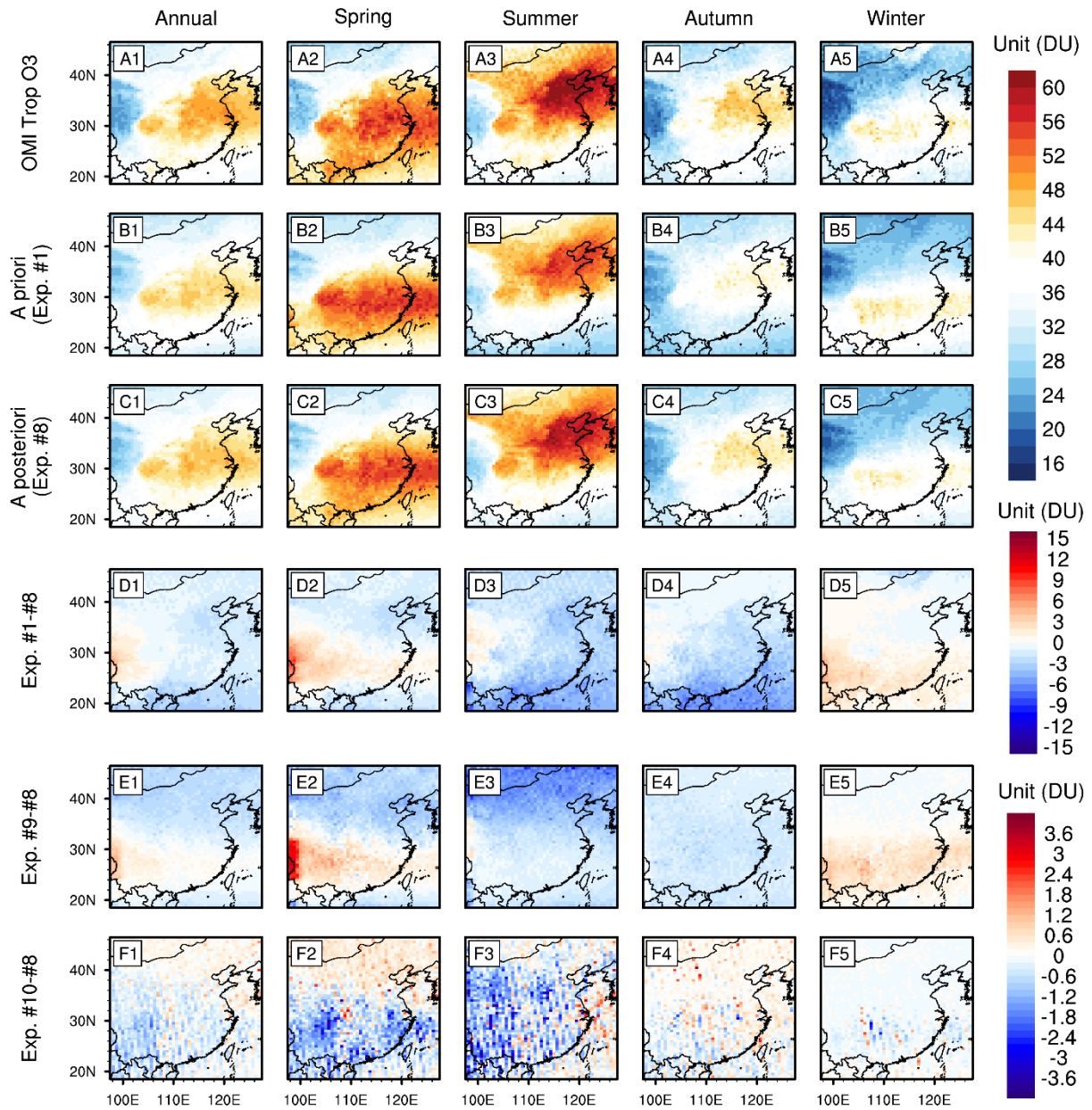
Fig. 7. Tropospheric O₃ columns in 2015-2020 (annual and seasonal averages) from (A1-A5) OMI observations; (B1-B5) GEOS-Chem a priori simulation (Exp. #1); (C1-C5) GEOS-Chem a posteriori simulation by assimilating OMI O₃ observations (Exp. #8). (D1-D5) Bias in the a priori simulations (Exp. #1 minus #8). (E1-E5) Effects of optimization on regional O₃ background conditions (Exp. #9 minus #8); (F1-F5) Effects of the usage of row-isolated data (Exp. #10 minus #8). The output O₃ profiles are convolved with OMI averaging kernels.
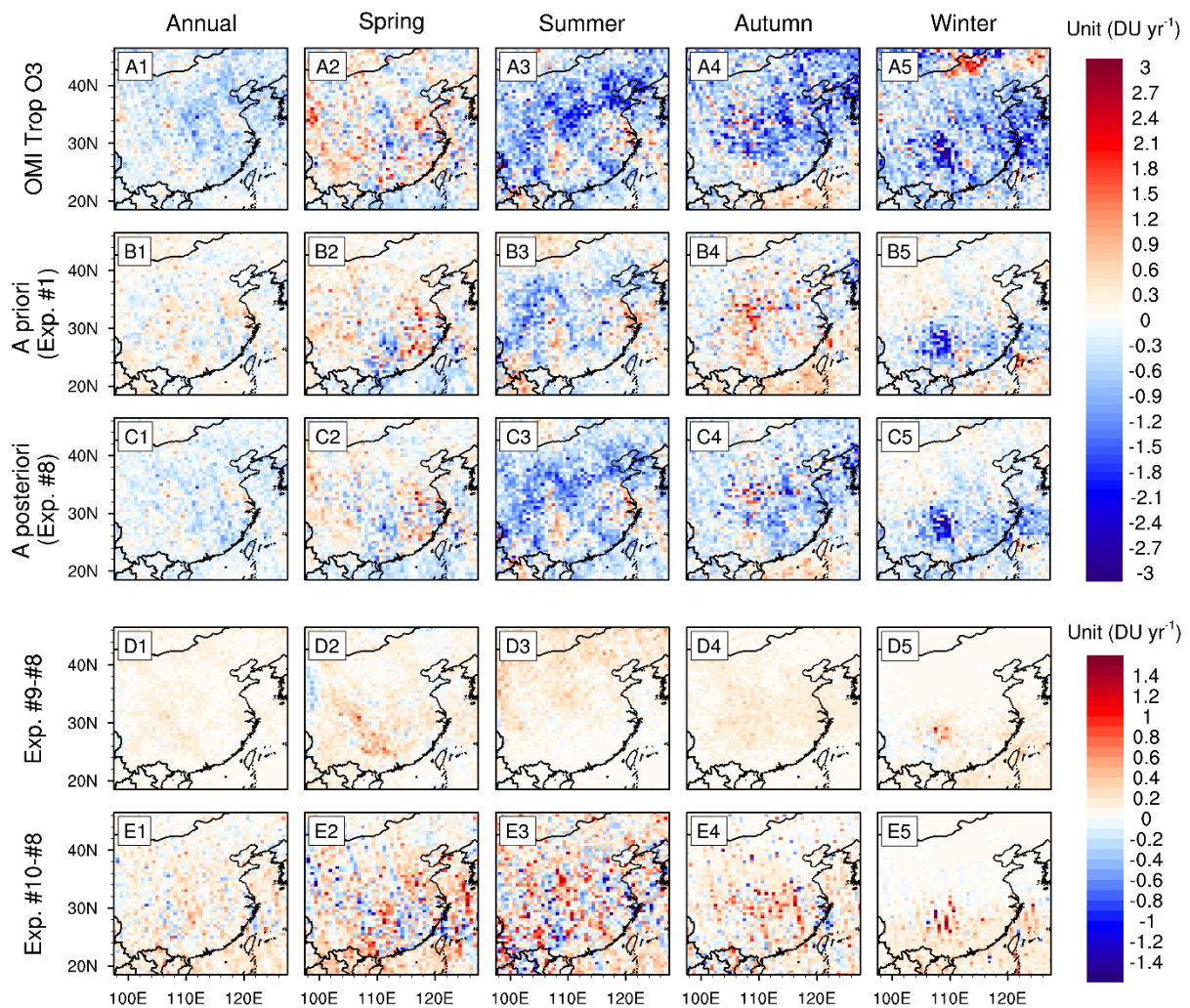
Fig. 8. Trends of tropospheric O₃ columns in 2015-2020 (annual and seasonal averages) from (A1-A5) OMI observations; (B1-B5) GEOS-Chem a priori simulation (Exp. #1); (C1-C5) GEOS-Chem a posteriori simulation by assimilating OMI O₃ observations (Exp. #8). (D1-D5) Effects of optimization on regional O₃ background conditions (Exp. #9 minus #8); (E1-E5) Effects of the usage of row-isolated data (Exp. #10 minus #8). The output O₃ profiles are convolved with OMI averaging kernels.
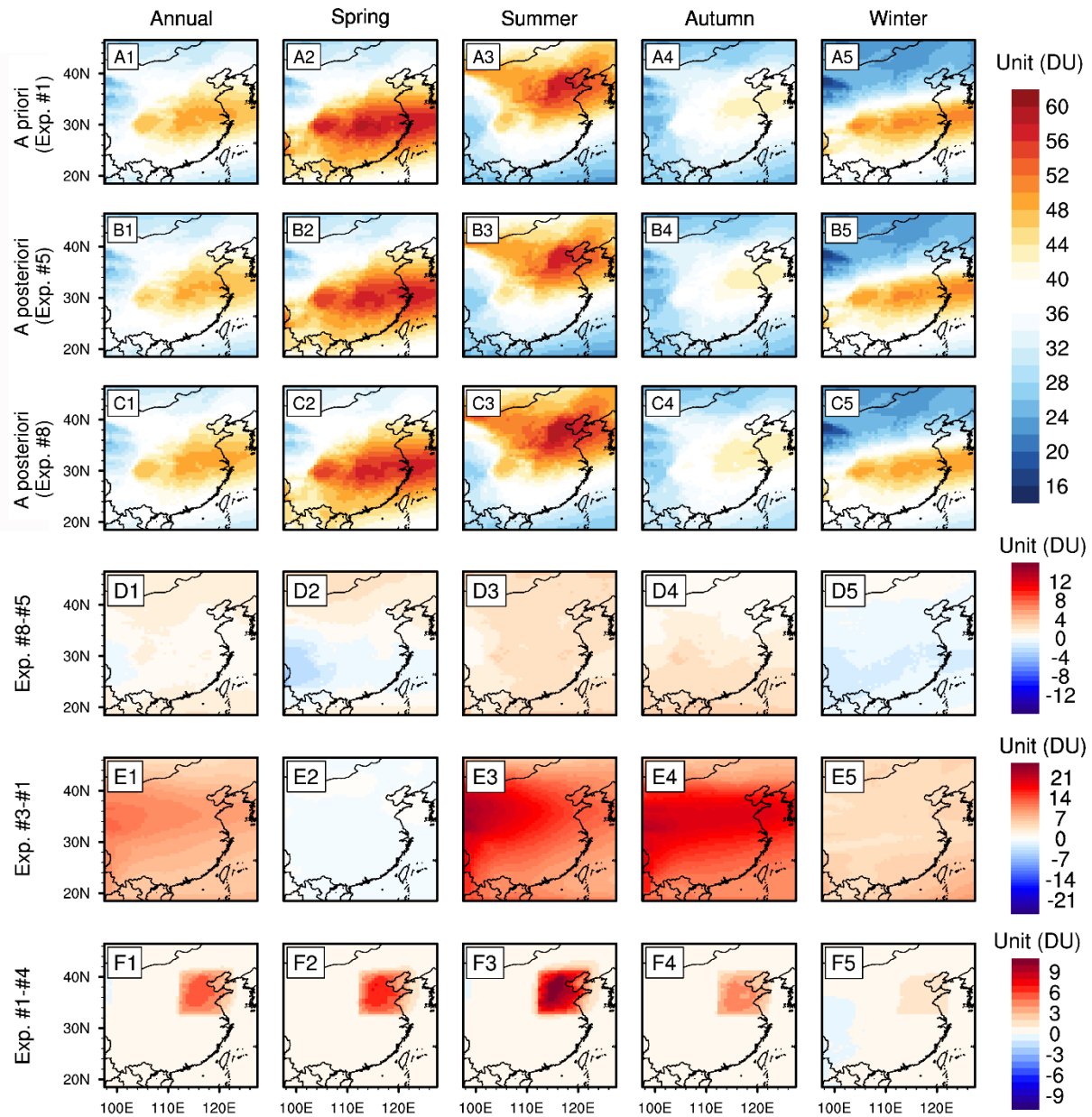
Fig. 9. Tropospheric O_3 columns in 2015-2020 (annual and seasonal averages) from (A1-A5) GEOS-Chem a priori simulation (Exp. #1); (B1-B5) Assimilations of MEE surface O_3 observations (Exp. #5); (C1-C5) Assimilations of OMI O_3 observations (Exp. #8). (D1-D5) Difference in tropospheric O_3 columns calculated by OMI-based assimilations minus MEE-based assimilations (Exp. #8 minus #5). (E1-E5) Effects of seasonal variabilities in background O_3 (Exp. #3 minus #1); (F1-F5) Effects of O_3 formation within the North China Plain PBL (Exp. #1 minus #4). The output O_3 profiles are NOT convolved with OMI averaging kernels.

Fig. 10. Trends of tropospheric O₃ columns in 2015-2020 (annual and seasonal averages) from (A1-A5) GEOS-Chem a priori simulation (Exp. #1); (B1-B5) Assimilations of MEE surface O₃ observations (Exp. #5); (C1-C5) Assimilations of OMI O₃ observations (Exp. #8). (D1-D5) Effects of interannual variabilities in background O₃ (Exp. #1 minus #2). The output O₃ profiles are NOT convolved with OMI averaging kernels.